

# Synergistic interplay between Dirac fermions and long-wavelength order parameters in graphene-insulator heterostructures

Xin Lu,<sup>1</sup> Shihao Zhang,<sup>1</sup> Zheng Vitto Han,<sup>2,3</sup> and Jianpeng Liu<sup>1,4,\*</sup>

<sup>1</sup>*School of Physical Science and Technology, ShanghaiTech University, Shanghai 201210, China*

<sup>2</sup>*State Key Laboratory of Quantum Optics and Quantum Optics Devices, Institute of Opto-Electronics, Shanxi University, 030006 Taiyuan, China*

<sup>3</sup>*Collaborative Innovation Center of Extreme Optics, Shanxi University, 030006 Taiyuan, China*

<sup>4</sup>*ShanghaiTech laboratory for topological physics, ShanghaiTech University, Shanghai 201210, China*

In this work, we theoretically study the electronic structure, topological properties, and interaction effects of the low-energy Dirac electrons in band-aligned heterostructures consisted of graphene and some correlated insulating substrates. By virtue of the band alignment, charge carriers can be transferred from graphene to the insulating substrate under the control of gate voltages. This may yield a long-wavelength charge order at the surface of the substrate through the Wigner-crystallization mechanism. The long-wavelength charge order in turn exerts a superlattice Coulomb potential to the Dirac electrons in graphene, which reduces the non-interacting Fermi velocity, such that  $e$ - $e$  Coulomb interactions would play an important role. Consequently, the Dirac points are spontaneously gapped out by interactions leading to a sublattice polarized insulator state. Meanwhile, the Fermi velocities around the Dirac points are drastically enhanced to more than twice of the bare value by interaction effects, which can give rise to large Landau-level spacing with robust quantization plateaus of Hall resistivity under weak magnetic fields and at high temperatures. We have further performed high-throughput first principles calculations, and suggested a number of promising insulating materials as candidate substrates for graphene, which could realize the gapped Dirac state concomitant with low-field, high-temperature quantum Hall effects.

*Introduction.* — Graphene hosts 2D massless Dirac electrons with linear dispersions in the vicinity of two inequivalent  $K$  and  $K'$  valleys in the Brillouin zone (BZ) [1, 2]. As the two Dirac points act as sources of Berry curvatures, graphene is considered as a precursor of topological phases of matter. For example, imposing a time-reversal breaking “mass term” to the Dirac electrons in graphene may open up a gap at the Dirac points, rendering nonzero Chern number [3]. Such linear dispersions and topological properties of Dirac cones bestow various intriguing physical properties to graphene including the relativistic Landau levels, the Klein tunnelling effects, and the nontrivial edge states, etc. [2]. Moreover, graphene is also considered as a promising candidate for the next-generation field effect devices due to its high carrier mobility. Therefore, many efforts have been made to engineer graphene’s Dirac-type band structures through electrical methods.

Transition metal oxides (TMOs) and transition metal chalcogenides (TMCs) have also stimulated significant research interests over the past few decades due to the diverse correlated states discovered in these systems such as Mott insulators [4] and unconventional superconductivity [5, 6]. In particular, by virtue of multiple electronic degrees of freedom in TMOs, they may exhibit various spontaneous symmetry breaking states which are characterized by charge, orbital, and/or spin order parameters [7, 8]. Some of these TMOs may exhibit long-wavelength order parameters such as the magnetic skyrmion lattice state [9–12] and the incommensurate charge-density wave state [13–16].

An open question is what would happen if some long-

wavelength order parameters (such as charge and magnetic orders) in an insulating TMO or TMC substrate are coupled in proximity to the Dirac electrons in graphene, as schematically shown in Fig. 1(a). On the one hand, the electronic structures of graphene may be changed due to the proximity coupling to the long-wavelength order parameters, which would impose a long-wavelength potential to the Dirac electrons and would strongly renormalize the single-particle band structure in the graphene layer. On the other hand, the properties of the order parameters may also be changed due to the couplings with the itinerant Dirac electrons, which may lead to different order states (e.g., order parameters with different wave lengths) in the TMO or TMC substrate. For example, recent experiments in graphene-CrOCl heterostructure [17] and graphene-CrI<sub>3</sub> heterostructure [18] shows robust quantum Hall effect under magnetic fields as weak as  $\sim 0.2$  T, with a gapped state at the charge neutrality point (CNP); while experiments on TaS<sub>2</sub>-graphene heterostructure [19] reveal a proximity-induced CDW state in the graphene layer. Therefore, the mutual couplings between graphene and TMO (TMC) may lead to a synergistic interplay between the Dirac electrons and the local order parameters, giving rise to new physics that cannot be realized if the two systems were isolated from each other.

Motivated by recent experiments on graphene-CrOCl [17], graphene-CrI<sub>3</sub> [18], and graphene-TaS<sub>2</sub> heterostructures [19], in this work we theoretically study the heterostructure system with monolayer graphene stacked on top of an insulating substrate whose band edge is energetically close to the Dirac points of graphene. We

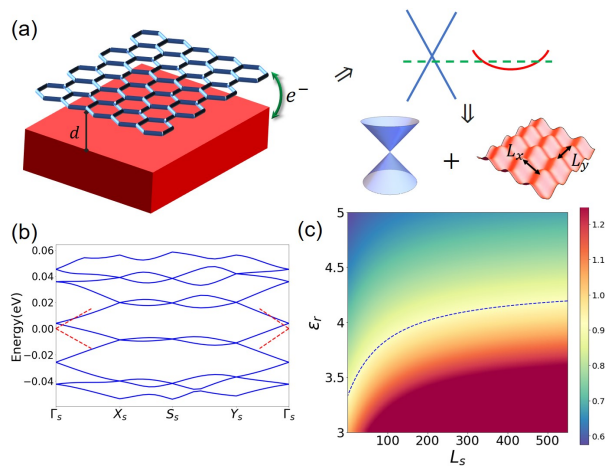


FIG. 1: (a) Schematic of a band-aligned graphene-insulator heterostructure: blue honeycomb lattice represents graphene sheet and red rectangular box is the insulating substrate, where charge carriers can be transferred between them due to the band alignment. We model such a system by Dirac fermions moving in a periodic charge-ordered superlattice. (b) shows the non-interacting band structure by blue solid lines after solving the Hamiltonian Eq. (1) in a rectangular superlattice with  $r = 1.2$  of  $L_x = 600 \text{ \AA}$ . For comparison, we also show by red dashed lines the Dirac cones without any renormalization. (c) shows the calculated effective fine structure constant  $\alpha(L_s, \epsilon_d)$  for our model Hamiltonian, where the dashed line marks the critical value  $\alpha_c \approx 0.92$  above which the Dirac point may be gapped out by interactions.

consider the situation of gate-controlled charge transfer from graphene to the otherwise insulating substrate, which introduces slight carrier dopings at the band edge with large effective mass (as for  $\text{CrOCl}$  or  $\text{CrI}_3$ ). Then, electron-electron ( $e-e$ ) interaction effects at the band edge of the substrate may drive the system into a long-wavelength Wigner-crystal-like state or charge-ordered state, whose period is typically inversely proportional to the transferred carrier density, thus can be controlled by gate voltages. We ask how the low-energy spectrum of graphene is changed due to the coupling with the long-wavelength charge order, and reciprocally how the properties of the charge ordered state can be changed due to the coupling to graphene. We find that, the long-wavelength charge order in the substrate would impose a superlattice Coulomb potential to the Dirac electrons in graphene, which would first suppress the non-interacting Fermi velocity of the Dirac cone, thus promote gap opening at the Dirac points triggered by  $e-e$  interactions. Meanwhile, concomitant with the gap opening at Dirac points, the Fermi velocities around the CNP are also dramatically enhanced by  $e-e$  interactions, which may lead to large Landau-level spacing and robust quantum Hall

effects under extremely low magnetic fields. The gap opening at the Dirac points, which is tunable by vertical gate voltages, would be promising for a potential field-effect transistor device; while the drastically enhanced Fermi velocity around CNP (by  $e-e$  Coulomb interactions) would give rise to robust quantum Hall effects under tiny magnetic fields  $\sim 0.2 \text{ T}$  which persists to high temperatures  $\sim 100 \text{ K}$  [17].

The two seemingly contradictory phenomena, namely the gap opening and the enhancement of Fermi velocity, both turn out to result from the  $e-e$  interactions in graphene, the effects of which are significantly boosted by the coupling to the long-wavelength charge order in the insulating substrate. Moreover, the superlattice constant of the interaction-triggered crystalline charge order is closely related to the Fermi surface of the non-interacting band of the substrate, the size of which can be tuned externally by virtue of the interface carrier transfer from graphene back to the surface band of the insulating substrate. In particular, the Fermi surface can vary from 2D like to quasi-1D like, leading to long-wavelength charge ordered state with different wavelength ( $L_s$ ) and anisotropy parameter ( $r$ ) on top of the insulating substrate [20]. Then, such ordered state would exert a superlattice potential with variable  $L_s$  on graphene via long-range Coulomb interactions. The wavelength and anisotropy of the charge ordered lattice can be changed accordingly (e.g., in a Wigner crystal picture), which in turn modifies the electronic structure, topological properties, and correlation effects of the graphene layer. Such a synergistic interplay between Dirac fermions and the long-wavelength charge order at the surface of the substrate would give rise to diverse correlated and topological phases as discussed throughout this work.

*Model Hamiltonian.* — To describe the graphene-insulator heterostructure, we consider a model Hamiltonian consisted of a graphene part, an insulator substrate part, and the coupling between them. As we are interested in the low energy electronic properties, graphene's band structure is modeled by the low-energy Dirac cones around the  $K$  and  $K'$  valleys. The long-wavelength charge ordered state in the substrate is considered as a charge insulator, with the electrons being frozen to form a superlattice and their orbitals have negligible overlaps with those of the Dirac electrons in the graphene layer. Thus, long-wavelength charge order of the substrate does not directly contribute to low-energy electronic properties, but it is coupled to the graphene layer merely via long-range Coulomb interactions to exert a superlattice potential on the Dirac electrons in graphene. Since the superlattice constant, characterized by a length scale  $L_s$  ( $\approx 50 \text{ \AA}$ ) [17], is much larger than the lattice constant of graphene, we can safely omit the intervalley coupling and model graphene as two separate continua of Dirac fermions from two valleys.

Accordingly, we can construct an effective single-

particle Hamiltonian, schematically shown in Fig. 1(a), for Dirac fermions in graphene that are coupled with an effective background superlattice potential (arising from Coulomb interactions with the long-wavelength charge order in the TMO substrate)

$$H_0^\mu(\mathbf{r}) = \hbar v_F \mathbf{k} \cdot \boldsymbol{\sigma}^\mu + U_d(\mathbf{r}) \quad (1)$$

where  $\boldsymbol{\sigma}^\mu$  are the Pauli matrices ( $\mu\sigma_x, \sigma_y$ ) with the valley index  $\mu = \pm 1$ ,  $v_F$  is the non-interacting Fermi velocity of graphene, and  $U_d(\mathbf{r})$  is the background superlattice potential with the period  $U_d(\mathbf{r}) = U_d(\mathbf{r} + \mathbf{L}_s)$ . The superlattice of the long-wavelength charge order defined by  $\mathbf{L}_s$  is set to be a rectangular one in our calculations, whose anisotropy is characterized by  $r = L_y/L_x$  with  $L_{x,y}$  being the lattice constant in the  $x, y$ -direction, respectively. As a result, the superlattice potential  $U_d(\mathbf{r})$  would fold Dirac cones into its small BZ forming subbands and opening up a gap at the boundary of the supercell BZ, as shown in Fig. 1(b) for a rectangular superlattice with  $r = 1.2$  in valley  $K$  ( $\mu = 1$ ) with  $L_s = 600$  Å. The energy degeneracies from folding are all lifted by  $U_d$ , whose Fourier component reads [20]

$$U_d(\mathbf{Q}) = \frac{e^2}{\epsilon_0 \epsilon_d \Omega_0} \cdot \frac{e^{-Qd_0}}{Q} \quad (2)$$

where  $\mathbf{Q} \neq \mathbf{0}$  is the reciprocal lattice vector associated with  $\mathbf{L}_s$ ,  $\Omega_0 = L_x L_y$  is the area of the primitive cell of the superlattice. The Coulomb potential  $U_d$ , screened by a dielectric constant  $\epsilon_d$ , decays exponentially in the reciprocal space  $\sim \exp(-Qd_0)$ , where  $d_0$  is the distance between the substrate surface and graphene monolayer. Since the Dirac point is protected by the product of  $C_{2z}$  and time-reversal ( $\mathcal{T}$ ) symmetry, which is preserved for the superlattice potential  $U_d$  [Eq. (2)], the degeneracy at the Dirac point survives. However,  $U_d$  breaks chiral symmetry of the band structure as the superlattice potential commutes with the chirality operator  $\sigma_z$ . Furthermore, the Fermi velocities near the Dirac points of the subbands are suppressed by  $U_d$  [21], which is clearly visible for  $L_s = 600$  Å, as shown in Fig. 1(b).

While it is highly desirable to open a gap at the Dirac points in graphene for the purpose of field-effect device fabrication, 2D superlattice potential alone cannot gap out Dirac points in graphene as the system still preserves  $C_{2z}\mathcal{T}$  symmetry. However, the Dirac points can be unstable against  $e$ - $e$  Coulomb interactions (with the spontaneous breaking of  $C_{2z}\mathcal{T}$  symmetry) once the Fermi velocity of the non-interacting band structure is suppressed below a threshold, which can be assisted by the superlattice potential from the long-wavelength charge order. One of the best illustrations is twisted bilayer graphene (TBG) [22], in which the Fermi velocity is strongly suppressed around the “magic angle” due to the long-wavelength moiré potential, leading to moiré flat bands. Then  $e$ - $e$  Coulomb interactions would drive the

system into spontaneous symmetry breaking insulating states at partial integer fillings of the flat bands [23–42]

Inspired by the physics in magic-angle TBG, here we further calculate the Fermi velocity of the superlattice subbands around the Dirac point using second-order perturbation theory, which reads

$$v_F(\hat{\mathbf{k}}) = v_F^0 \left( 1 - \sum_{\mathbf{Q} \neq \mathbf{0}} \frac{2|U_d(\mathbf{Q})|^2 \sin^2 \theta_{\hat{\mathbf{k}}, \mathbf{Q}}}{\hbar v_F^0 |\mathbf{Q}|^2} \right), \quad (3)$$

where  $v_F^0 = 5.229 \text{ eV} \cdot \text{Å}$  is the non-interacting Fermi velocity of graphene,  $\theta_{\hat{\mathbf{k}}, \mathbf{Q}}$  is the angle between unit vector  $\hat{\mathbf{k}}$  and reciprocal vector  $\mathbf{Q}$ . Assuming a square superlattice  $L_x = L_y = L_s$ , keeping only the leading-order Fourier component of  $U_d(|\mathbf{Q}| = 2\pi/L_s)$ , we find that the Fermi velocity  $v_F(L_s, \epsilon_d)$  and the corresponding effective fine-structure constant  $\alpha(L_s, \epsilon_d) = e^2/(4\pi\epsilon_0\epsilon_d\hbar v_F(L_s, \epsilon_d))$  can be expressed as

$$v_F(L_s, \epsilon_d) \approx v_F^0 \left( 1 - \frac{4\alpha_0^2}{\pi^2 \epsilon_d^2} e^{-\frac{4\pi d_0}{L_s}} \right) \quad (4a)$$

$$\alpha(L_s, \epsilon_d) \approx \frac{\alpha_0}{\epsilon_d} \frac{1}{1 - 4\alpha_0^2 e^{-4\pi d_0/L_s}/(\epsilon_d^2 \pi^2)} \quad (4b)$$

where  $\alpha_0 = e^2/4\pi\epsilon_0\hbar v_F^0 = 2.75$  is the effective fine structure constant of free-standing graphene. It is already evident from a simple second-order perturbation treatment that the effective fine structure constant is sensitive to both dielectric constant of the substrate  $\epsilon_d$  and the superlattice constant  $L_s$ , while the latter can be tuned by the carrier density at the surface of the insulating substrate transferred from graphene. A practical numerical calculation of  $\alpha(L_s, \epsilon_d)$  is presented in Fig. 1(c). We see that there is a substantial region in the  $(L_s, \epsilon_d)$  phase space with  $\alpha(L_s, \epsilon_d) > \alpha_c \approx 0.92$  [43], which indicates that the Dirac-semimetal phase of graphene may no longer be stable against  $e$ - $e$  interactions within this regime.

*e-e interaction effects.* — This motivates us to include  $e$ - $e$  interactions in the graphene layer in our model, which are treated by Hartree-Fock approximation [20]. Although several previous theoretical studies [44–47] predict the onset of interacting gapped state in graphene, to the best of our knowledge no gap at the CNP has been experimentally observed in graphene yet [48, 49]. This can be attributed to the interaction-enhanced Fermi velocity near the CNP [50–53], the screening of  $e$ - $e$  interactions, disorder effects, etc., all of which may prohibit the emergence of a gapped state [44]. Nevertheless, analogous to TBG, the subbands in our system with reduced non-interacting Fermi velocity would quench the kinetic energy and further promote the  $e$ - $e$  interaction effects in graphene. A recent experimental work has indeed found that the Dirac point in graphene is gapped if graphene is stacked on top of a CrOCl substrate, and the latter may form a long-wavelength charge order on its surface

through a Wigner-crystal-like instability due to the carrier transfer from graphene [17].

Our unrestricted Hartree-Fock calculations [20] confirm precisely the argument above, and are consistent with the aforementioned experimental result [17]. Considering graphene is made into a device controlled by top and bottom gates, so that we can employ a double-gate screened Coulomb interaction for electrons in graphene:

$$V(\mathbf{q}) = \frac{e^2 \tanh(qd_s)}{2\Omega_0 \epsilon_d \epsilon_0 q}, \quad (5)$$

with a background dielectric constant  $\epsilon_d = 3-5$  and the thickness between two gates  $d_s = 400 \text{ \AA}$ . Then, the Coulomb interactions are written in the subband eigenfunction basis. As interaction effects are most prominent around the CNP, we project the Coulomb interactions onto only a low-energy subspace including five valence and five conduction subbands ( $n_{\text{cut}} = 5$ ) that are closest to the Dirac points for each valley and spin. We adopt a mesh of  $18 \times 18$   $\mathbf{k}$  points to sample the mini BZ of the superlattice.

To incorporate the influences of Coulomb interactions from the high-energy remote bands, which are omitted in previous Hartree-Fock calculations [45, 47] for graphene, we rescale the Fermi velocity within the low-energy window of the effective Hamiltonian using the formula derived from the renormalization group (RG) approach [2, 20, 44, 52, 54]

$$v_F^* = v_F^0 \left( 1 + \frac{\alpha_0}{4\epsilon_r} \log \frac{E_c}{E_c^*} \right) \quad (6)$$

where  $E_c^*$  is the low-energy window within which the Hartree-Fock calculations are to be performed, and  $E_c$  is an overall energy cut-off above which the Dirac-fermion description to graphene is no longer valid. Equivalently, the ratio between  $E_c$  and  $E_c^*$  is replaced here by  $L_s/(n_{\text{cut}} a)$  with graphene's honeycomb lattice constant  $a$  and the charge-order superlattice constant  $L_s$ . Unlike TBG [55], other parameters of the effective Hamiltonian [Eq. (1)] such as  $U_d$ , are unchanged under the RG flow since their RG corrections are of higher order, thus can be neglected [20]. Feeding with the initial conditions in the form of order parameters involving all possible valley, spin, and sublattice degrees of freedom, we self-consistently calculate the ground-state energies and density matrices for all the different types of symmetry-breaking states, based on which the Hartree-Fock single-particle spectrum can be further obtained [20].

We first study the Hartree-Fock single-particle spectrum of graphene coupled to the rectangular superlattice potential with  $r = 1.2$  and  $50 \text{ \AA} \leq L_s \leq 600 \text{ \AA}$ , with  $\epsilon_d = 3$ . Here, we consider two different filling factors (denoted by  $\nu$ ): exactly at the CNP ( $\nu = 0$ ) and a slight hole doping with respect to CNP ( $\nu \approx -0.003$ ). The result for the slight electron doping case is similar to that for the slight hole doping [20]. First of all,

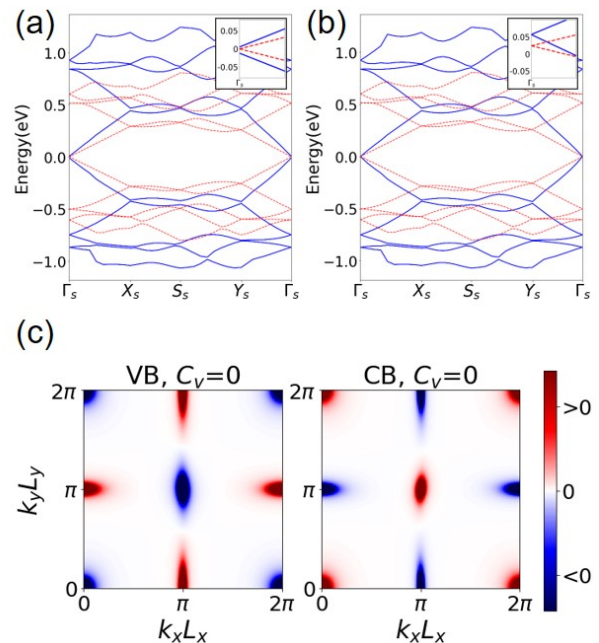


FIG. 2: (a) and (b) show by blue solid lines the Hartree-Fock single-particle spectrum of  $L_s = 50 \text{ \AA}$  at the CNP and with a slight hole doping, respectively. For comparison, their corresponding non-interacting band structures are also represented by red dashed lines in the same panel. The inset in them zooms in energy at the vicinity of the Dirac points. (c) Distribution of Berry curvature in the superlattice's BZ of the lowest valence and conduction band for  $r = 1.2$  and  $L_s = 50 \text{ \AA}$  in valley  $K$  with their valley Chern number  $C_v$ . The result for the valley  $K'$  is exactly opposite [20].

when  $\nu = 0$ , a gap can be opened up due to interaction effects, leading to two nearly degenerate insulating states, one is polarized in sublattice and the other polarized in valley. Then, intervalley Coulomb interactions would split such degeneracy, and the sublattice polarized insulator with zero Chern number becomes the unique ground state, consistent with previous studies [47]. The gap hits 17 meV when  $L_s = 50 \text{ \AA}$ , and decreases to 1.7 meV for  $L_s = 200 \text{ \AA}$ , and eventually becomes nearly gapless (0.15 meV) when  $L_s = 600 \text{ \AA}$  with  $\epsilon_r = 3$ . (see also Table I). This can be understood by Eq. (6): larger  $L_s$  leads to stronger renormalization of the Fermi velocity by the Coulomb potential exerted on the low-energy electrons from the occupied remote bands outside the low-energy window, thus favors kinetic energy and suppresses gap opening. It is worthwhile to emphasize again that the renormalization of Fermi velocity [Eq. (6)] by itself is also an interaction effect. The single-particle excitation spectrum is also significantly altered by Coulomb interactions within the low-energy window, as shown in Fig. 2(a) for  $L_s = 50 \text{ \AA}$  and  $\epsilon_d = 3$ , with filling  $\nu = 0$ . The

particle-hole asymmetry of the spectrum becomes more prominent. The Fermi velocity of the low-energy conduction band becomes different from that of the valence band. More saliently, although the superlattice potential  $U_d$  suppresses Fermi velocity in graphene [see Eq. (4b)],  $e$ - $e$  interactions can compensate such effects. The Fermi velocity is not only enhanced by the Coulomb potentials of the remote energy bands outside the low-energy window [Eq. (6)], but also further boosted by  $e$ - $e$  interactions within the low energy window  $E_c^* \sim n_{\text{cut}} \hbar v_F 2\pi / L_s$ . Eventually, the Fermi velocity is magnified up to twice of the non-interacting value of free-standing graphene ( $v_F^0$ ). Inherited the anisotropy from the underlying superlattice, the Fermi velocity is renormalized more heavily in the  $y$ -direction than in the  $x$ -direction. We note that the essential results discussed above, i.e., the gap opening at CNP and the concomitant drastic enhancement of Fermi velocity, remain robust for different types of the background superlattices. Specifically, we have also performed calculations for the case of triangular charge-ordered superlattices, which lead to qualitatively the same conclusions [20].

TABLE I: Gap opened at the CNP ( $\nu = 0$ ) and the ratio between interaction-enhanced Fermi velocity  $v_F^*$  and the non-interacting one  $v_F$  for different  $L_s = 50, 200, 600$  Å with fixed  $r = 1.2$ .

$L_s$ (Å)	50	200	600
Gap at $\nu = 0.0$ (meV)	17	1.7	0.15
$v_F^*/v_F^0$ at $\nu = -0.003$	2.1	1.8	1.7

When the system is slightly hole doped with  $\nu = -0.003$ , the Dirac points would remain gapless, as shown in Fig. 2(b). Moreover, the Fermi velocity would be even more dramatically enhanced ( $\sim 2.1 v_F^0$ ) than that for the  $\nu = 0$  case ( $\sim 1.8 v_F^0$ ), as shown in Table I. This perfectly explains the recent experiment in gated controlled graphene-CrOCl and -CrI<sub>3</sub> heterostructure, in which a gap has been observed at the CNP, and in the meantime the Fermi velocity around CNP is significantly enhanced compared to the non-interacting value, such that robust quantum Hall effect can be observed under vertical magnetic fields as weak as  $\sim 0.1$ – $1$  T [17, 18].

*Topological Properties.* — We further study the topological properties of our model Hamiltonian. Different from magic-angle TBG [56–60], the low-energy subbands for graphene coupled to a rectangular superlattice potential  $U_d(\mathbf{r})$  with small anisotropy ( $r \sim 1$ ) turns out to be topologically trivial. To be specific, in Fig. 2(c) we show the Berry curvature distribution of the highest valence and the lowest conduction band of valley  $K$  in the mini BZ of the superlattice with  $L_x = 50$  Å and  $r = L_y/L_x = 1.2$ . We see that the Berry curvature is mostly concentrated at the band crossing points, i.e., the four high symmetry points  $\Gamma_s, S_s, X_s,$  and  $Y_s$ . The

contributions from the  $\Gamma_s$  and the  $S_s$  points are exactly compensated by those from the  $X_s$  and  $Y_s$  points, resulting in a band with zero Chern number. This is anticipated because the superlattice potential is non-chiral in the sense that it is coupled equally to the two sublattices of graphene. This remains true even including  $e$ - $e$  interactions [20].

Hence, it is unexpected that changing the anisotropy  $r$  and the lattice size  $L_s$  of the superlattice potential  $U_d$  can make the subbands topological. For example, keeping  $L_x = 50$  Å but with  $r = 3.0$ , the valley Chern number of the low-energy subbands become nonzero. For valley  $K$ , the highest valence band and lowest conduction band now have a Chern number  $C = \pm 1$ , respectively. As shown in Fig. 3(a), besides the four high symmetry points, it appears another two “hot spots” (annotated by green circles) along the line connecting  $\Gamma_s$  and  $X_s$ , leading to non-zero valley Chern number. Such contribution stems from a new crossing point between the low-energy valence and conduction bands along the  $k_x$ -direction through changing merely the anisotropy parameter  $r$ , as shown in Fig. 3(c) with red dot in green circle. Alternatively, we find that changing  $L_s$  can also control the valley Chern number of the subbands, since  $L_s$  is encoded in the superlattice potential [see Eq. (2)]. For example, with  $r = 3$  and  $L_s = 600$  Å, as shown in Fig. 3(b), while the highest valence band remains topological with non-zero valley Chern number 1 for valley  $K$  with the two aforementioned crossing points (green circles) merely moving to  $X_s$ , the lowest conduction band turns out to be topologically trivial. This is due to two new band crossing points (orange circles) close to the  $Y_s$ - $S_s$  line between the lowest and the second lowest conduction bands, as annotated by red dots in an orange circle in Fig. 3(d). Such topologically nontrivial bands are particularly surprising for our system, since the Dirac fermions are coupled to a “trivial” superlattice potential coupled identically on two sublattices, different from the case of magic-angle TBG. Thus, the nontrivial topology must arise by virtue of the intrinsic Berry phases of the Dirac cones.

*Materials realization.* — As mentioned earlier, such a model study of Dirac fermions coupled to a background superlattice potential with tunable lattice constant and anisotropy is closely related to CrOCl-graphene and CrI<sub>3</sub>-graphene heterostructure systems. The superlattice potential arises from long-range Coulomb interactions between electrons in graphene and the long-wavelength charge order at the surface of CrOCl (or CrI<sub>3</sub>) substrate, which emerges as a CDW-like or Wigner-crystal-type instability due to the slight carrier doping transfer from graphene to the surface conduction band of CrOCl or CrI<sub>3</sub>, and is highly tunable by vertical electric fields [20]. This is plausible since electrons in the top surface states (transferred from graphene) have a very low density ( $\sim 10^{12}$  cm<sup>-2</sup>, as deduced from the nominal doping



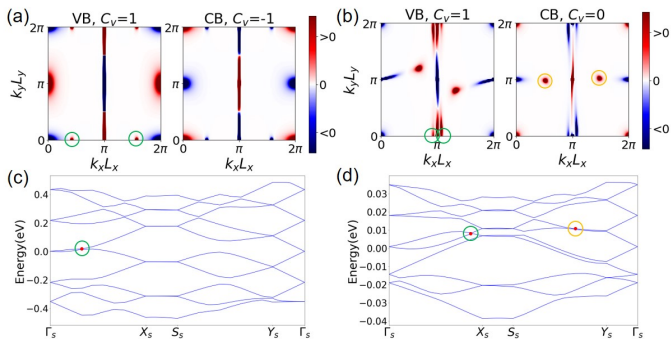


FIG. 3: (a) and (b) shows the distribution of Berry curvature in the  $r = 3$  superlattice's BZ of the lowest valence and conduction band in valley  $K$  for  $L_s = 50$  and  $600 \text{ \AA}$ , respectively. Their corresponding valley Chern number are also given on the top of each panel. (c) and (d) are the non-interacting band structure of the  $r = 3$  superlattice with  $L_s = 50$  and  $600 \text{ \AA}$ . (e) Valley Chern number of the highest valence and the lowest conduction band in the valley  $K$  varying the anisotropy parameter  $r$  from 1 to 10 with  $L_s = 50 \text{ \AA}$ .

in Ref. 17). Consequently, the associated dimensionless Wigner-Seitz radius turns out to be  $r_s \sim 39.4\text{--}65.7$  with an effective mass  $m = 1.308 m_0$  near the surface conduction band minimum of CrOCl, assuming a dielectric constant  $\epsilon_d = 3\text{--}5$  [20]. This  $r_s$  value is clearly above the threshold value ( $\sim 30$ ) for the onset of the Wigner crystal state [61].

There is no reason that the scenario sketched above should be restricted to the CrOCl or CrI<sub>3</sub> substrate. As long as the substrate material is insulating with either the conduction band minimum (CBM) or valence band maximum (VBM) being energetically close to the Dirac points of graphene, charges could be easily transferred between graphene and the surface of the substrate material by gate voltages below the disruptive threshold. Furthermore, it is more likely to form long-wavelength ordered state at the surface of the substrate (with slight carrier doping) if the material has large effective masses at the CBM or VBM, such that the system would be more susceptible to Coulomb interactions. Driven by the interplay between  $e\text{-}e$  Coulomb interactions in graphene and the superlattice potential exerted by the long-wavelength charge order, the gapped Dirac points and the dramatically enhanced Fermi velocities could be realized concomitantly.

To find such desirable substrates for graphene for the demonstration of similar physical phenomena as those reported in CrOCl- and CrI<sub>3</sub>-graphene heterostructures, we have performed high-throughput first principles calculations based on density functional theory for various insulating van der Waals materials. Our high-throughput filtering starts from the 2D materials compu-

tational database [62], and we only focus at those with bulk van der Waals structures which have been previously synthesized in laboratory. This ensures that it is experimentally feasible to exfoliate few layers from their bulk sample and then stack them on graphene to form heterostructures. Based on these guidelines, we find eleven suitable candidate materials (including CrOCl and CrI<sub>3</sub>), whose CBM and VBM energy positions, dielectric constants ( $\epsilon_r$ ), effective masses at the band edges, and the corresponding Wigner-Seitz radii ( $r_s$ ) are listed in Table II. Clearly, the Wigner-Seitz radii of these materials at the band edges (estimated under slight doping concentration  $n = 10^{12} \text{ cm}^{-2}$ ) are all above the threshold of forming a Wigner-crystal state ( $r_s \gtrsim 30$ ). Additionally, the energy bands of these insulating substrate materials can be easily shifted using vertical displacement fields, such that charge transfer between graphene and the substrate can be controlled by non-disruptive displacement fields. These results would provide experimentally promising insulator-graphene heterostructure candidates, where gapped Dirac state emerges concomitantly with drastically enhanced Fermi velocity.

TABLE II: Candidate substrate materials for the graphene-insulator heterostructure systems. The dielectric constants  $\epsilon_r$  [63–65], conduction band minimum position ( $E_{\text{CBM}}$ ), valence band maximum position ( $E_{\text{VBM}}$ ), the corresponding effective mass  $m_{\text{CBM}}$  or  $m_{\text{VBM}}$  of the band edge that is energetically closer to the Dirac point, and the dimensionless Wigner-Seitz radius  $r_s = \sqrt{2}m/(\epsilon_d m_0 a_B \sqrt{\pi n})$  estimated with a slight doping concentration  $n = 10^{12} \text{ cm}^{-2}$ , where  $a_B$  is the Bohr radius. The energy position of the Dirac point in graphene is set to zero. “bi” and “tri” stand for bilayer and trilayer configurations, respectively.

Materials	$\epsilon_d$	$E_{\text{CBM}}$	$E_{\text{VBM}}$	$m_{\text{CBM/VBM}}$	$r_s$
AgScP <sub>2</sub> S <sub>6</sub> (bi)	3.67	0.07 eV	-1.89 eV	$3.939 m_0$	161.1
AgScP <sub>2</sub> Se <sub>6</sub> (bi)	4.06	0.15 eV	-1.37 eV	$2.632 m_0$	97.3
IrBr <sub>3</sub> (bi)	6.53	0.23 eV	-1.43 eV	$8.083 m_0$	185.8
IrI <sub>3</sub> (bi)	7.59	0.33 eV	-0.95 eV	$1.756 m_0$	34.7
YI <sub>3</sub> (tri)	3.45	0.53 eV	-2.1 eV	$2.123 m_0$	92.4
YBr <sub>3</sub> (tri)	6.78	0.68 eV	-3.15 eV	$2.764 m_0$	61.2
ReSe <sub>2</sub> (bi)	6.38	0.32 eV	-0.83 eV	$1.823 m_0$	42.9
ScOCl (bi)	5.27	0.21 eV	-4.04 eV	$3.287 m_0$	93.6
PbO (bi)	8.47	2.02 eV	-0.03 eV	$11.885 m_0$	210.7
CrI <sub>3</sub> (bi)	3.00	-0.32 eV	-1.58 eV	$2.018 m_0$	101.0
CrOCl (bi)	3-5	-0.13 eV	-3.26 eV	$1.308 m_0$	39.4-65.7

*Conclusions.* — In conclusion, we have theoretically studied the interplay between the Dirac fermions and long-wavelength charge order in graphene-insulator heterostructure systems. We consider the situation that charge carriers can be transferred from graphene to the surface of the insulating substrate under the control of gate voltages, by virtue of the band alignment between the Dirac points in graphene and the CBM (or VBM)

of the insulator. The resultant slight carrier doping may yield a long-wavelength charge order through the Wigner crystallization mechanism at the surface of the substrate, which in turn exerts a superlattice potential to the Dirac electrons in graphene. The Dirac spectrum is then renormalized by the background superlattice potential with reduced non-interacting Fermi velocity, such that  $e$ - $e$  Coulomb interactions would play an important role. Consequently, the Dirac points are spontaneously gapped out by interactions leading to a sublattice polarized insulator state. Meanwhile, the Fermi velocities around the CNP in graphene are drastically enhanced to more than twice of the bare value by interaction effects, which can give rise to large Landau-level spacings with robust quantization plateaus of Hall resistivity under weak magnetic fields and at high temperatures. Our theory can perfectly explain the recent puzzling experiments in CrOCl-graphene and CrI<sub>3</sub>-graphene heterostructures. We have further performed high-throughput DFT calculations, and suggest a number of promising insulating materials as candidate substrates for graphene, which could realize the gapped Dirac state concomitant with low-field and high-temperature quantum Hall effects. Our work unveils a tip of the iceberg of the rich physics in graphene-insulator heterostructure systems, more exciting physical phenomena are yet to be explored in such graphene-based heterostructure systems.

---

\* liujp@shanghaitech.edu.cn

- [1] K. S. Novoselov, A. K. Geim, S. V. Morozov, D. Jiang, Y. Zhang, S. V. Dubonos, I. V. Grigorieva, and A. A. Firsov, *Science* **306**, 666 (2004), <https://science.sciencemag.org/content/306/5696/666.full.pdf>.
- [2] A. H. Castro Neto, F. Guinea, N. M. R. Peres, K. S. Novoselov, and A. K. Geim, *Rev. Mod. Phys.* **81**, 109 (2009).
- [3] F. D. M. Haldane, *Physical Review Letters* **61**, 2015 (1988).
- [4] M. Imada, A. Fujimori, and Y. Tokura, *Rev. Mod. Phys.* **70**, 1039 (1998).
- [5] P. A. Lee, N. Nagaosa, and X.-G. Wen, *Rev. Mod. Phys.* **78**, 17 (2006).
- [6] M. Sigrist and K. Ueda, *Rev. Mod. Phys.* **63**, 239 (1991).
- [7] Y. Tokura and N. Nagaosa, *Science* **288**, 462 (2000).
- [8] W. Witczak-Krempa, G. Chen, Y. B. Kim, and L. Balents, *Annual Review of Condensed Matter Physics* **5**, 57 (2014).
- [9] S. Seki, X. Yu, S. Ishiwata, and Y. Tokura, *Science* **336**, 198 (2012).
- [10] Z. S. Lim, H. Jani, T. Venkatesan, and A. Ariando, *MRS Bulletin*, 1 (2022).
- [11] T. Kurumaji, T. Nakaajima, V. Ukleev, A. Feoktystov, T.-h. Arima, K. Kakurai, and Y. Tokura, *Phys. Rev. Lett.* **119**, 237201 (2017).
- [12] Y. Tokura and N. Kanazawa, *Chemical Reviews* **121**, 2857 (2020).
- [13] M. Hossain, Z. Zhao, W. Wen, X. Wang, J. Wu, and L. Xie, *Crystals* **7**, 298 (2017).
- [14] H. Miao, R. Fumagalli, M. Rossi, J. Lorenzana, G. Seibold, F. Yakhou-Harris, K. Kummer, N. B. Brookes, G. D. Gu, L. Braicovich, G. Ghiringhelli, and M. P. M. Dean, *Phys. Rev. X* **9**, 031042 (2019).
- [15] A. Frano, S. Blanco-Canosa, E. Schierle, Y. Lu, M. Wu, M. Bluschke, M. Minola, G. Christiani, H. Habermeier, G. Logvenov, et al., *Nature materials* **15**, 831 (2016).
- [16] R. Zhao, Y. Wang, D. Deng, X. Luo, W. J. Lu, Y.-P. Sun, Z.-K. Liu, L.-Q. Chen, and J. Robinson, *Nano letters* **17**, 3471 (2017).
- [17] Y. Wang, X. Gao, K. Yang, P. Gu, B. Dong, Y. Jiang, K. Watanabe, T. Taniguchi, J. Kang, W. Lou, J. Mao, Y. Ye, Z. V. Han, K. Chang, J. Zhang, and Z. Zhang, *Flavoured quantum hall phase in graphene/crocl heterostructures* (2021).
- [18] C.-C. Tseng, T. Song, J. Suh, Z. Lin, K. Watanabe, T. Taniguchi, J.-H. Chu, D. Cobden, X. Xu, and M. Yankowitz, *Bulletin of the American Physical Society* (2022).
- [19] M. A. Altvater, S.-H. Hung, N. Tilak, C.-J. Won, G. Li, S.-W. Cheong, C.-H. Chung, H.-T. Jeng, and E. Y. Andrei, *Revealing the charge density wave proximity effect in graphene on 1t-tas2* (2022).
- [20] See supplementary information for more details.
- [21] C.-H. Park, L. Yang, Y.-W. Son, M. L. Cohen, and S. G. Louie, *Nature Physics* **4**, 213 (2008).
- [22] R. Bistritzer and A. H. MacDonald, *Proceedings of the National Academy of Sciences* **108**, 12233 (2011), <https://www.pnas.org/doi/pdf/10.1073/pnas.1108174108>.
- [23] Y. Cao, V. Fatemi, A. Demir, S. Fang, S. L. Tomarken, J. Y. Luo, J. D. Sanchez-Yamagishi, K. Watanabe, T. Taniguchi, E. Kaxiras, et al., *Nature* **556**, 80 (2018).
- [24] Y. Cao, V. Fatemi, S. Fang, K. Watanabe, T. Taniguchi, E. Kaxiras, and P. Jarillo-Herrero, *Nature* **556**, 43 (2018).
- [25] A. L. Sharpe, E. J. Fox, A. W. Barnard, J. Finney, K. Watanabe, T. Taniguchi, M. Kastner, and D. Goldhaber-Gordon, *Science* **365**, 605 (2019).
- [26] M. Serlin, C. Tschirhart, H. Polshyn, Y. Zhang, J. Zhu, K. Watanabe, T. Taniguchi, L. Balents, and A. Young, *Science* **367**, 900 (2020).
- [27] L. Balents, C. R. Dean, D. K. Efetov, and A. F. Young, *Nat. Phys.* **16**, 725 (2020).
- [28] E. Y. Andrei, D. K. Efetov, P. Jarillo-Herrero, A. H. MacDonald, K. F. Mak, T. Senthil, E. Tutuc, A. Yazdani, and A. F. Young, *Nat. Rev. Mater.* **6**, 201 (2021).
- [29] J. Liu and X. Dai, *Nature Reviews Physics* **3**, 367 (2021).
- [30] H. C. Po, L. Zou, A. Vishwanath, and T. Senthil, *Physical Review X* **8**, 031089 (2018).
- [31] J. Kang and O. Vafek, *Phys. Rev. Lett.* **122**, 246401 (2019).
- [32] M. Xie and A. H. MacDonald, *Phys. Rev. Lett.* **124**, 097601 (2020).
- [33] M. Angeli, E. Tosatti, and M. Fabrizio, *Physical Review X* **9**, 041010 (2019).
- [34] D. Wong, K. P. Nuckolls, M. Oh, B. Lian, Y. Xie, S. Jeon, K. Watanabe, T. Taniguchi, B. A. Bernevig, and A. Yazdani, *Nature* **582**, 198 (2020).
- [35] N. Bultinck, E. Khalaf, S. Liu, S. Chatterjee, A. Vishwanath, and M. P. Zaletel, *Physical Review X* **10**, 031034 (2020).

- [36] P. Stepanov, I. Das, X. Lu, A. Fahimniya, K. Watanabe, T. Taniguchi, F. H. Koppens, J. Lischner, L. Levitov, and D. K. Efetov, *Nature* **583**, 375 (2020).
- [37] U. Zondiner, A. Rozen, D. Rodan-Legrain, Y. Cao, R. Queiroz, T. Taniguchi, K. Watanabe, Y. Oreg, F. von Oppen, A. Stern, *et al.*, *Nature* **582**, 203 (2020).
- [38] J. Liu and X. Dai, *Physical Review B* **103**, 035427 (2021).
- [39] B. A. Bernevig, Z.-D. Song, N. Regnault, and B. Lian, *Phys. Rev. B* **103**, 205413 (2021).
- [40] B. Lian, Z.-D. Song, N. Regnault, D. K. Efetov, A. Yazdani, and B. A. Bernevig, *Phys. Rev. B* **103**, 205414 (2021).
- [41] Y. H. Kwan, G. Wagner, T. Soejima, M. P. Zaletel, S. H. Simon, S. A. Parameswaran, and N. Bultinck, *Phys. Rev. X* **11**, 041063 (2021).
- [42] S. Zhang, X. Lu, and J. Liu, *arXiv preprint arXiv:2109.11441* (2021).
- [43] O. V. Gamayun, E. V. Gorbar, and V. P. Gusynin, *Phys. Rev. B* **81**, 075429 (2010).
- [44] V. N. Kotov, B. Uchoa, V. M. Pereira, F. Guinea, and A. H. Castro Neto, *Rev. Mod. Phys.* **84**, 1067 (2012).
- [45] J. Jung and A. H. MacDonald, *Phys. Rev. B* **84**, 085446 (2011).
- [46] H.-K. Tang, J. N. Leaw, J. N. B. Rodrigues, I. F. Herbut, P. Sengupta, F. F. Assaad, and S. Adam, *Science* **361**, 570 (2018), <https://www.science.org/doi/pdf/10.1126/science.aao2934>.
- [47] M. Trushin and J. Schliemann, *Phys. Rev. Lett.* **107**, 156801 (2011).
- [48] D. C. Elias, R. Gorbachev, A. Mayorov, S. Morozov, A. Zhukov, P. Blake, L. Ponomarenko, I. Grigorieva, K. Novoselov, F. Guinea, *et al.*, *Nature Physics* **7**, 701 (2011).
- [49] C. Faugeras, S. Berciaud, P. Leszczynski, Y. Henni, K. Nogajewski, M. Orlita, T. Taniguchi, K. Watanabe, C. Forsythe, P. Kim, R. Jalil, A. K. Geim, D. M. Basko, and M. Potemski, *Phys. Rev. Lett.* **114**, 126804 (2015).
- [50] S. Das Sarma, E. H. Hwang, and W.-K. Tse, *Phys. Rev. B* **75**, 121406 (2007).
- [51] G. Borghi, M. Polini, R. Asgari, and A. MacDonald, *Solid State Communications* **149**, 1117 (2009), recent Progress in Graphene Studies.
- [52] J. Gonzalez, F. Guinea, and V. M. A. H., *Nuclear Physics B* **424**, 595 (1994).
- [53] T. Stauber, P. Parida, M. Trushin, M. V. Ulybyshev, D. L. Boyda, and J. Schliemann, *Phys. Rev. Lett.* **118**, 266801 (2017).
- [54] R. R. Nair, P. Blake, A. N. Grigorenko, K. S. Novoselov, T. J. Booth, T. Stauber, N. M. Peres, and A. K. Geim, *Science* **320**, 1308 (2008).
- [55] O. Vafek and J. Kang, *Phys. Rev. Lett.* **125**, 257602 (2020).
- [56] Z. Song, Z. Wang, W. Shi, G. Li, C. Fang, and B. A. Bernevig, *Phys. Rev. Lett.* **123**, 036401 (2019).
- [57] J. Ahn, S. Park, and B.-J. Yang, *Phys. Rev. X* **9**, 021013 (2019).
- [58] H. C. Po, L. Zou, T. Senthil, and A. Vishwanath, *Phys. Rev. B* **99**, 195455 (2019).
- [59] G. Tarnopolsky, A. J. Kruchkov, and A. Vishwanath, *Phys. Rev. Lett.* **122**, 106405 (2019).
- [60] J. Liu, J. Liu, and X. Dai, *Phys. Rev. B* **99**, 155415 (2019).
- [61] N. D. Drummond and R. J. Needs, *Phys. Rev. Lett.* **102**, 126402 (2009).
- [62] S. Haastруп, M. Strange, M. Pandey, T. Deilmann, P. S. Schmidt, N. F. Hinsche, M. N. Gjerding, D. Torelli, P. M. Larsen, A. C. Riis-Jensen, J. Gath, K. W. Jacobsen, J. J. Mortensen, T. Olsen, and K. S. Thygesen, *2D Mater.* **5**, 042002 (2018).
- [63] I. Petousis, W. Chen, G. Hautier, T. Graf, T. D. Schladt, K. A. Persson, and F. B. Prinz, *Phys. Rev. B* **93**, 115151 (2016).
- [64] I. Petousis, D. Mrdjenovich, E. Ballouz, M. Liu, D. Winston, W. Chen, T. Graf, T. D. Schladt, K. A. Persson, and F. B. Prinz, *Scientific Data* **4**, 160134 (2017).
- [65] K. Choudhary, K. F. Garrity, A. C. Reid, B. DeCost, A. J. Biacchi, A. R. H. Walker, Z. Trautt, J. Hatrck-Simpers, A. G. Kusne, A. Centrone, *et al.*, *npj Computational Materials* **6**, 1–13 (2020).
- [66] S. Zhang, X. Dai, and J. Liu, *Phys. Rev. Lett.* **128**, 026403 (2022).
- [67] B. Jariwala, D. Voiry, A. Jindal, B. A. Chalke, R. Bapat, A. Thamizhavel, M. Chhowalla, M. Deshmukh, and A. Bhattacharya, *Chemistry of Materials* **28**, 3352 (2016).
- [68] S. Yang, C. Wang, H. Sahin, H. Chen, Y. Li, S.-S. Li, A. Suslu, F. M. Peeters, Q. Liu, J. Li, and S. Tongay, *Nano Letters* **15**, 1660 (2015).
- [69] A. Arora, J. Noky, M. Drüppel, B. Jariwala, T. Deilmann, R. Schneider, R. Schmidt, O. Del Pozo-Zamudio, T. Stiehm, A. Bhattacharya, P. Krüger, S. Michaelis de Vasconcellos, M. Rohlfing, and R. Bratschitsch, *Nano Letters* **17**, 3202 (2017).
- [70] B. Huang, G. Clark, E. Navarro-Moratalla, D. R. Klein, R. Cheng, K. L. Seyler, D. Zhong, E. Schmidgall, M. A. McGuire, D. H. Cobden, W. Yao, D. Xiao, P. Jarillo-Herrero, and X. Xu, *Nature* **546**, 270 (2017).
- [71] B. Huang, G. Clark, D. R. Klein, D. MacNeill, E. Navarro-Moratalla, K. L. Seyler, N. Wilson, M. A. McGuire, D. H. Cobden, D. Xiao, W. Yao, P. Jarillo-Herrero, and X. Xu, *Nature Nanotechnology* **13**, 544 (2018).
- [72] S. Jiang, L. Li, Z. Wang, K. F. Mak, and J. Shan, *Nature Nanotechnology* **13**, 549 (2018).
- [73] D. R. Klein, D. MacNeill, J. L. Lado, D. Soriano, E. Navarro-Moratalla, K. Watanabe, T. Taniguchi, S. Manni, P. Canfield, J. Fernández-Rossier, and P. Jarillo-Herrero, *Science* **360**, 1218 (2018).
- [74] N. Sivadas, S. Okamoto, X. Xu, C. J. Fennie, and D. Xiao, *Nano Letters* **18**, 7658 (2018).
- [75] In our DFT+ $U$  calculations, the on-site Hubbard  $U = 5.48$  eV for the Cr  $3d$  orbitals is used in the calculations, and the non-spherical contributions from the gradient corrections are taken into consideration.
- [76] S. Lee, P. Colombet, G. Ouvrard, and R. Brec, *Inorganic Chemistry* **27**, 1291 (1988).
- [77] S. Seidlmayer, R. Wehrich, and A. Pfitzner, *Zeitschrift für anorganische und allgemeine Chemie* **632**, 2122 (2006).
- [78] K. Brodersen, G. Thiele, H. Ohnsorge, I. Recke, and F. Moers, *Journal of the Less Common Metals* **15**, 347 (1968).
- [79] K. Brodersen, *Angewandte Chemie International Edition in English* **7**, 148 (1968).
- [80] L. B. Asprey, T. K. Keenan, and F. H. Kruse, *Inorganic Chemistry* **3**, 1137 (1964).
- [81] H. MATTAUSCH, J. B. HENDRICKS, R. EGER, J. D. CORBETT, and A. SIMON, *Chemischer Informations-*



- dienst **11** (1980).
- [82] J. Wildervanck and F. Jelinek, *Journal of the Less Common Metals* **24**, 73 (1971).
- [83] E. Garcia, J. D. Corbett, J. E. Ford, and W. J. Vary, *Inorganic Chemistry* **24**, 494 (1985).
- [84] J. Moreau, J. M. Kiat, P. Garnier, and G. Calvarin, *Phys. Rev. B* **39**, 10296 (1989).
-

# Supplemental Information for “Synergistic interplay between Dirac fermions and long-wavelength orders in graphene-insulator heterostructures”

## S1. NON-INTERACTING HAMILTONIAN FOR A GRAPHENE-INSULATOR HETEROSTRUCTURE

The Hamiltonian for a graphene-insulator heterostructure can be always divided into three parts: graphene part  $H_G$ , the insulating substrate part  $H_S$  and the coupling between them  $H_{G-S}$ . The graphene part can be suitably described by a tight-binding model since we focus on the low-energy physics. As we have explained in the main text, with slight carrier doping band edge, the insulator substrate is supposed to form a long-wavelength charge order on the interface near graphene sheet thanks to Coulomb interactions between electrons occupying the band edge of the insulating substrate (transferred from graphene layer). The insulator substrate part is then modeled by a 2D Hamiltonian for electrons hopping on a 2D superlattice which forms an Wigner-crystal-like or long-wavelength charge ordered insulator state at some proper filling, whose geometry is determined by the long-wavelength order at the interface. Explicitly, the graphene part  $H_G$  and the insulator substrate part  $H_S$  can be generally written as

$$\hat{H}_G = \sum_{\mathbf{k}, \sigma, \alpha, \alpha'} \gamma_{\alpha, \alpha'}(\mathbf{k}) \hat{c}_{\sigma\alpha}^\dagger(\mathbf{k}) \hat{c}_{\sigma\alpha'}(\mathbf{k}) \quad (S1)$$

$$\hat{H}_S = \sum_{\tilde{\mathbf{k}}, \sigma} \eta(\tilde{\mathbf{k}}) \hat{d}_{\sigma}^\dagger(\tilde{\mathbf{k}}) \hat{d}_{\sigma}(\tilde{\mathbf{k}}) \quad (S2)$$

where  $\hat{c}_{\mathbf{k}, \alpha, \sigma}$  ( $\hat{c}_{\mathbf{k}, \alpha, \sigma}^\dagger$ ) and  $\hat{d}_{\tilde{\mathbf{k}}, \sigma}$  ( $\hat{d}_{\tilde{\mathbf{k}}, \sigma}^\dagger$ ) are fermionic annihilation (creation) operators for electrons in graphene and the insulator substrate, respectively. In the lower index of these operators,  $\alpha$  is the sublattice index for the bipartite lattice of graphene and  $\sigma$  is the spin degree of freedom of electrons. To emphasize the fact that graphene and the insulator substrate have different lattices and thus different Brillouin zone, we denote  $\mathbf{k}$  and  $\tilde{\mathbf{k}}$  as the wavevectors in the Brillouin zone of graphene and that of the long-wavelength superlattice in the substrate, respectively. In our calculations, the lattice for  $H_S$  is set to rectangular or triangular, which does not qualitatively change our results.

Since electrons have negligible probability to hop between graphene and the insulator substrate due to rather large distance  $d$  between two sheets in the  $z$ -direction ( $d \sim 7 \text{ \AA}$  from DFT calculations in CrOCl-graphene heterostructure), we suppose that electrons from two sheets are coupled only via long-ranged Coulomb interactions. Unlike  $H_G$  and  $H_S$ , such long-ranged Coulomb interactions are more easily written in real space. In terms of field operators  $\hat{\psi}(\mathbf{r})$ , the inter-sheet coupling reads

$$\hat{H}_{G-S} = \int d^2\mathbf{r} d^2\mathbf{r}' \sum_{\sigma, \sigma'} \hat{\psi}_{c, \sigma}^\dagger(\mathbf{r}) \hat{\psi}_{d, \sigma'}^\dagger(\mathbf{r}') V(|\mathbf{r} - \mathbf{r}' + d\hat{\mathbf{z}}|) \hat{\psi}_{d, \sigma'}(\mathbf{r}') \hat{\psi}_{c, \sigma}(\mathbf{r}) \quad (S3)$$

where  $V(|\mathbf{r} - \mathbf{r}' + d\hat{\mathbf{z}}|)$  is the 3D long-ranged Coulomb potential  $e^2/4\pi\epsilon_0\epsilon_d r$  and electrons in graphene and the insulating substrate are described by the field operators with lower index  $c$  and  $d$ , respectively. Here  $\epsilon_0$  is the vacuum permittivity and  $\epsilon_d$  is the dimensionless relative dielectric constant of the insulating substrate. In the spirit of tight-binding formalism, we write the field operators in terms of Wannier functions

$$\hat{\psi}_{c, \sigma}^\dagger(\mathbf{r}) = \sum_{i, \alpha} \phi_\alpha^*(\mathbf{r} - \mathbf{a}_i - \boldsymbol{\tau}_\alpha) \chi_\sigma^\dagger \hat{c}_{i, \sigma\alpha}^\dagger \quad (S4)$$

$$\hat{\psi}_{d, \sigma}^\dagger(\mathbf{r}) = \sum_{i, \alpha} \tilde{\phi}^*(\mathbf{r} - \mathbf{R}_i) \chi_\sigma^\dagger \hat{d}_{i, \sigma}^\dagger \quad (S5)$$

where  $\phi_\alpha$  and  $\tilde{\phi}$  are Wannier functions localized on the graphene and the insulator substrate Bravais lattice sites, which are described by  $\mathbf{a}_i$  and  $\mathbf{R}_i$ , respectively. Here  $\alpha$  refers to the sublattice index in graphene and  $\boldsymbol{\tau}_\alpha$  is the vector denoting the position of the  $\alpha$ th sublattice inside the unit-cell. The spin degrees of freedom is included by the index  $\sigma$  and also explicitly by spinor  $\chi_\sigma$ . The Hamiltonian  $H_{G-S}$  in the Wannier basis reads

$$\hat{H}_{G-S} = \sum_{\substack{\sigma, \sigma' \\ \alpha, \alpha'}} \sum_{\substack{i, i' \\ j, j'}} U_{i\alpha j, i'\alpha' j'}^{\sigma\sigma'} \hat{c}_{i, \sigma\alpha}^\dagger \hat{d}_{j, \sigma'}^\dagger \hat{d}_{j', \sigma'} \hat{c}_{i', \sigma\alpha'} \quad (S6)$$

with

$$U_{i\alpha j, i'\alpha' j'}^{\sigma\sigma'} = \int d^2\mathbf{r} d^2\mathbf{r}' \phi_\alpha^*(\mathbf{r} - \mathbf{a}_i - \boldsymbol{\tau}_\alpha) \tilde{\phi}^*(\mathbf{r} - \mathbf{R}_j) V(|\mathbf{r} - \mathbf{r}' + d\hat{\mathbf{z}}|) \tilde{\phi}(\mathbf{r}' - \mathbf{R}_{j'}) \phi_{\alpha'}(\mathbf{r} - \mathbf{a}_{i'} - \boldsymbol{\tau}_{\alpha'}) \chi_\sigma^\dagger \chi_{\sigma'}^\dagger \chi_{\sigma'} \chi_\sigma. \quad (S7)$$

If Wannier functions are so localized such that

$$\begin{aligned}
\phi_\alpha^*(\mathbf{r} - \mathbf{a}_i - \boldsymbol{\tau}_\alpha)\phi_{\alpha'}(\mathbf{r} - \mathbf{a}_{i'} - \boldsymbol{\tau}_{\alpha'}) &\approx 0 && \text{if } (i, \alpha) \neq (i', \alpha') \\
\tilde{\phi}^*(\mathbf{r} - \mathbf{R}_j)\tilde{\phi}(\mathbf{r} - \mathbf{R}_{j'}) &\approx 0 && \text{if } j \neq j' \\
|\phi_\alpha(\mathbf{r} - \mathbf{a}_i - \boldsymbol{\tau}_\alpha)|^2 &\approx \delta^{(2)}(\mathbf{r} - \mathbf{a}_i - \boldsymbol{\tau}_\alpha) \\
|\tilde{\phi}(\mathbf{r} - \mathbf{R}_j)|^2 &\approx \delta^{(2)}(\mathbf{r} - \mathbf{R}_j)
\end{aligned}$$

with  $\delta^{(2)}(\mathbf{r})$  is the 2D Dirac  $\delta$ -function distribution, we can simplify the previous expression to

$$U_{i\alpha j, i'\alpha' j'}^{\sigma\sigma'} = U_{i\alpha j}\delta_{i, i'}\delta_{\alpha, \alpha'}\delta_{j, j'} \quad (\text{S8})$$

with  $\delta_{\mu, \nu}$  is the Kronecker delta and

$$U_{i\alpha j} = V(|\mathbf{a}_i + \boldsymbol{\tau}_\alpha - \mathbf{R}_j + d\hat{\mathbf{z}}|). \quad (\text{S9})$$

Then, we write  $H_{G-S}$  in reciprocal space using the following Fourier transformation

$$\hat{c}_{i, \sigma\alpha} = \frac{1}{\sqrt{N_c}} \sum_{\mathbf{k}} e^{i\mathbf{k}\cdot\mathbf{a}_i} \hat{c}_{\sigma\alpha}(\mathbf{k}) \quad (\text{S10})$$

$$\hat{d}_{i, \sigma} = \frac{1}{\sqrt{N_d}} \sum_{\tilde{\mathbf{k}}} e^{i\tilde{\mathbf{k}}\cdot\mathbf{R}_i} \hat{d}_\sigma(\tilde{\mathbf{k}}) \quad (\text{S11})$$

where  $N_c$  and  $N_d$  are the number of lattice sites for electron in graphene and the insulator substrate, respectively. The Hamiltonian  $H_{G-S}$  in the basis of  $\hat{c}_{\sigma\alpha}(\mathbf{k})$  and  $\hat{d}_\sigma(\tilde{\mathbf{k}})$  reads

$$\hat{H}_{G-S} = \frac{1}{N_c N_d} \sum_{\substack{\sigma, \sigma' \\ i, \alpha, j}} \sum_{\substack{\mathbf{k}, \tilde{\mathbf{k}} \\ \tilde{\mathbf{k}}, \tilde{\mathbf{k}}'}} U_{i\alpha j} e^{i(\mathbf{k}' - \mathbf{k})\cdot(\mathbf{a}_i - \mathbf{R}_j)} e^{i(\mathbf{k}' - \mathbf{k} + \tilde{\mathbf{k}}' - \tilde{\mathbf{k}})\cdot\mathbf{R}_j} \hat{c}_{\sigma\alpha}^\dagger(\mathbf{k}) \hat{d}_{\sigma'}^\dagger(\tilde{\mathbf{k}}) \hat{d}_{\sigma'}(\tilde{\mathbf{k}}') \hat{c}_{\sigma\alpha}(\mathbf{k}'). \quad (\text{S12})$$

Now we first define  $\tilde{\mathbf{R}} = \mathbf{a}_i - \mathbf{R}_j$ , and let  $\mathbf{k}' - \mathbf{k} = \mathbf{q} = \tilde{\mathbf{q}} + \mathbf{G}$ , where  $\mathbf{G}$  is a reciprocal vector of the long-wavelength ordered superlattice and  $\tilde{\mathbf{q}}$  is the wavevector within the superlattice Brillouin zone. Then we take use of the identity  $\sum_j e^{i(\tilde{\mathbf{k}}' - \tilde{\mathbf{k}} + \mathbf{q})\cdot\mathbf{R}_j} = \sum_j e^{i(\tilde{\mathbf{k}}' - \tilde{\mathbf{k}} + \tilde{\mathbf{q}} + \mathbf{G})\cdot\mathbf{R}_j} = N_d \delta_{\tilde{\mathbf{k}}' - \tilde{\mathbf{k}}, \tilde{\mathbf{q}}}$ , Eq. (S12) can be simplified as

$$\hat{H}_{G-S} = \sum_{\substack{\sigma, \sigma' \\ \alpha}} \sum_{\substack{\mathbf{k}, \tilde{\mathbf{k}} \\ \tilde{\mathbf{q}}, \tilde{\mathbf{G}}}} \tilde{V}(\tilde{\mathbf{q}} + \mathbf{G}) \hat{c}_{\sigma\alpha}^\dagger(\mathbf{k}) \hat{d}_{\sigma'}^\dagger(\tilde{\mathbf{k}}) \hat{d}_{\sigma'}(\tilde{\mathbf{k}} + \tilde{\mathbf{q}}) \hat{c}_{\sigma\alpha}(\mathbf{k} - \tilde{\mathbf{q}} - \mathbf{G}) \quad (\text{S13})$$

The coupling  $\tilde{V}(\tilde{\mathbf{q}} + \mathbf{G})$  reads

$$\begin{aligned}
\tilde{V}(\tilde{\mathbf{q}} + \mathbf{G}) &= \frac{1}{N_c} \sum_i V(|\mathbf{a}_i + \boldsymbol{\tau}_\alpha - \mathbf{R}_j + d\hat{\mathbf{z}}|) e^{-i(\tilde{\mathbf{q}} + \mathbf{G})\cdot(\mathbf{a}_i - \mathbf{R}_j)} \\
&= \frac{1}{N_c} \sum_{\tilde{\mathbf{R}}} V(|\tilde{\mathbf{R}} + \boldsymbol{\tau}_\alpha + d\hat{\mathbf{z}}|) e^{-i(\tilde{\mathbf{q}} + \mathbf{G})\cdot\tilde{\mathbf{R}}} \\
&= \frac{1}{N_d} \int \frac{d^2 r}{\Omega_d} V(|\mathbf{r} + \boldsymbol{\tau}_\alpha + d\hat{\mathbf{z}}|) e^{-i(\tilde{\mathbf{q}} + \mathbf{G})\cdot\mathbf{r}} \\
&= \frac{e^2}{2\epsilon_0 \epsilon_d N_d \Omega_d} \frac{e^{-|\tilde{\mathbf{q}} + \mathbf{G}|d}}{|\tilde{\mathbf{q}} + \mathbf{G}|}
\end{aligned} \quad (\text{S14})$$

where  $\Omega_d$  is the area of the unit-cell of the surface superlattice of the substrate. In the third line of the above derivation, we smear the sum over  $\tilde{\mathbf{R}} = \mathbf{a}_i - \mathbf{R}_j$  by replacing it with an integral over the surface  $S = N_d \Omega_d = N_c \Omega_c$  with  $\Omega_c$  the area of graphene's unit-cell since we are interested in the physics in the length scale of the superlattice  $\{\mathbf{R}_j\}$ , which is supposed to much larger than that of graphene. Finally, the last line is the 2D partial Fourier transformation of the 3D Coulomb potential.

Since we focus on the low-energy physics around the Dirac cones of graphene, we can attribute valley index  $\mu$  to electrons in graphene and neglect intervalley coupling thanks to the exponential decay of  $\tilde{V}(\mathbf{q})$  so that

$$\hat{H}_{G-S} = \sum_{\sigma, \sigma'} \sum_{\alpha} \sum_{\substack{\mathbf{k}, \tilde{\mathbf{k}} \\ \tilde{\mathbf{q}}, \mathbf{G}}} \tilde{V}(\tilde{\mathbf{q}} + \mathbf{G}) \sum_{\mu} \hat{c}_{\sigma\mu\alpha}^{\dagger}(\mathbf{k}) \hat{d}_{\sigma'}^{\dagger}(\tilde{\mathbf{k}}) \hat{d}_{\sigma'}(\tilde{\mathbf{k}} + \tilde{\mathbf{q}}) \hat{c}_{\sigma\mu\alpha}(\mathbf{k} - \tilde{\mathbf{q}} - \mathbf{G}). \quad (\text{S15})$$

In the meantime, the Hamiltonian for graphene only  $H_G$  [see Eq. (S2)] can be divided into two valley sectors

$$\hat{H}_G = \sum_{\mathbf{k}, \sigma, \alpha, \alpha', \mu} (\hbar v_F \mathbf{k} \cdot \boldsymbol{\sigma}^{\mu})_{\alpha, \alpha'} \hat{c}_{\sigma\alpha}^{\dagger}(\mathbf{k}) \hat{c}_{\sigma\alpha'}(\mathbf{k}) \quad (\text{S16})$$

where  $\boldsymbol{\sigma}^{\mu} = (\mu\sigma_x, \mu\sigma_y)$  with  $\sigma_{x,y}$  are the Pauli matrices and the valley index  $\mu = \pm 1$ .

In the Hartree approximation by pairing  $c$  and  $d$  separately, we have

$$\hat{H}_{G-S} = \sum_{\sigma, \alpha, \mu} \sum_{\mathbf{k}, \mathbf{G}} \tilde{V}(\mathbf{G}) \sum_{\tilde{\mathbf{k}}, \sigma'} \langle \hat{d}_{\sigma'}^{\dagger}(\tilde{\mathbf{k}}) \hat{d}_{\sigma'}(\tilde{\mathbf{k}}) \rangle \hat{c}_{\sigma\alpha\mu}^{\dagger}(\mathbf{k}) \hat{c}_{\sigma\alpha\mu}(\mathbf{k} - \mathbf{G}). \quad (\text{S17})$$

Since the long-wavelength charge order state is insulating presumably with two spin degenerate electrons occupying each supercell, we have

$$\sum_{\tilde{\mathbf{k}}, \sigma'} \langle \hat{d}_{\sigma'}^{\dagger}(\tilde{\mathbf{k}}) \hat{d}_{\sigma'}(\tilde{\mathbf{k}}) \rangle = 2N_d. \quad (\text{S18})$$

Writing  $\mathbf{k} = \tilde{\mathbf{k}} + \mathbf{G}$  with  $\mathbf{G}$  in the superlattice reciprocal lattice, the final form of the coupling between graphene and insulating substrate used in our calculations reads

$$\hat{H}_{G-S} = \sum_{\sigma, \alpha, \mu} \sum_{\substack{\mathbf{G}, \mathbf{Q} \\ \in \{\mathbf{G}_i\}}} \tilde{U}_d(\mathbf{Q}) \hat{c}_{\sigma\mu\alpha, \mathbf{G}+\mathbf{Q}}^{\dagger}(\tilde{\mathbf{k}}) \hat{c}_{\sigma\mu\alpha, \mathbf{G}}(\tilde{\mathbf{k}}). \quad (\text{S19})$$

where

$$\tilde{U}_d(\mathbf{Q}) = \frac{e^2}{\epsilon_0 \epsilon_d \Omega_d} \frac{e^{-|\mathbf{Q}|d}}{|\mathbf{Q}|} \quad (\text{S20})$$

In the meantime, we integrate out the Hamiltonian for insulating substrate  $H_S$  [see Eq. (S2)] so that it becomes a constant charge density, which is omitted in our calculations. To wrap up, we get the effective non-interacting Hamiltonian in continuum in the valley  $\mu$

$$H_0^{\mu}(\mathbf{r}) = \hbar v_F \mathbf{k} \cdot \boldsymbol{\sigma}^{\mu} + U_d(\mathbf{r}) \quad (\text{S21})$$

where the Fourier component of  $U_d(\mathbf{r})$  is precisely  $\tilde{U}_d(\mathbf{G})$  [see Eq. (S20)] with  $\mathbf{G}$  in the reciprocal lattice of the underlying insulating substrate's surface superlattice.

In our numerical implementations, the lattice of insulating substrate is set to be rectangular or triangular, from which we obtain qualitatively the same correlated states in the graphene layer. The range of  $\{\mathbf{G}_i\}$  is limited to  $|n_x|, |n_y| \leq 4$  with  $\mathbf{G} = n_x \mathbf{g}_x + n_y \mathbf{g}_y$ .  $\mathbf{g}_{x,y}$  are the two reciprocal lattice vectors for the rectangular lattice of insulating substrate. The sum over  $\mathbf{Q}$  in Eq. (S19) stops at the limit  $|n_x| + |n_y| \leq 2$ .

## S2. RENORMALIZATION GROUP DERIVATIONS

The derivation shown in this section is inspired from Ref. 55. The e-e Coulomb interaction operator in our derivations is written as

$$\hat{V}_{\text{int}} = \frac{1}{2} \int d^2\mathbf{r} d^2\mathbf{r}' V_c(\mathbf{r} - \mathbf{r}') \hat{\rho}(\mathbf{r}) \hat{\rho}(\mathbf{r}') \quad (\text{S22})$$

where  $V_c(\mathbf{r}) = e^2/4\pi\epsilon_0\epsilon_d r$  and  $\hat{\rho}(\mathbf{r})$  is the density operator of electrons at  $\mathbf{r}$ . The Hamiltonian Eq. (S21) is defined at some high energy cut-off  $\pm E_c$ . We focus in the valley  $\mu = +1$  by the virtue of which the derivation for the valley

$\mu = -1$  is immediate and the results are identical. Remember that the parameters  $v_F$  and  $\tilde{U}_d(G)$  should be thought of as being fixed by a measurement at  $E_c$  without e-e interactions. This also amounts to  $\hat{\rho}(\mathbf{r}) = \hat{\psi}^\dagger(\mathbf{r})\hat{\psi}(\mathbf{r})$  with the non-interacting field operator  $\hat{\psi}(\mathbf{r})$

$$\hat{\psi}(\mathbf{r}) = \sum_{\substack{\sigma, n, \mathbf{k}; \\ |\epsilon_{n, \mathbf{k}}| \leq E_c}} \phi_{\sigma n \mathbf{k}}(\mathbf{r}) \hat{c}_{\sigma n}(\mathbf{k}) \quad (\text{S23})$$

where  $\phi_{\sigma n \mathbf{k}}(\mathbf{r})$  is the wavefunction of an eigenstate of the non-interacting Hamiltonian  $H_0$  [see Eq. (S21)] with energy  $\epsilon_{n, \mathbf{k}}$  and its associated annihilation operator is  $\hat{c}_{\sigma n}(\mathbf{k})$ .

### Electron-electron interaction in a lower energy window

Now we change the cut-off  $E_c$  to a smaller one  $E'_c$  and see how these parameters are modified by  $\hat{V}_{\text{int}}$ .  $\hat{V}_{\text{int}}$  can be treated perturbatively when  $E'_c$  is much larger than any other energy scale in the system. To do so, we split the field operator  $\hat{\psi}(\mathbf{r}) = \hat{\psi}^{<}(\mathbf{r}) + \hat{\psi}^{>}(\mathbf{r})$  where

$$\hat{\psi}^{<}(\mathbf{r}) = \sum_{\substack{\sigma, n, \mathbf{k}; \\ |\epsilon_{n, \mathbf{k}}| \leq E'_c}} \phi_{\sigma n \mathbf{k}}(\mathbf{r}) \hat{c}_{\sigma n}(\mathbf{k}) \quad (\text{S24})$$

$$\hat{\psi}^{>}(\mathbf{r}) = \sum_{\substack{\sigma, n, \mathbf{k}; \\ E'_c < |\epsilon_{n, \mathbf{k}}| \leq E_c}} \phi_{\sigma n \mathbf{k}}(\mathbf{r}) \hat{c}_{\sigma n}(\mathbf{k}). \quad (\text{S25})$$

$$(\text{S26})$$

Then, we integrate out the fast modes  $\hat{\psi}^{>}(\mathbf{r})$  in the expansion of  $\hat{\rho}(\mathbf{r})\hat{\rho}(\mathbf{r}')$ . Note that  $\hat{\psi}^{>}(\mathbf{r})$  and  $\hat{\psi}^{>\dagger}(\mathbf{r})$  must appear equal times in each terms of the expansion otherwise it would vanish by taking the non-interacting mean value  $\langle \dots \rangle_0$ . Explicitly, these terms are retained up to a constant:

$$\begin{aligned} \hat{\rho}(\mathbf{r})\hat{\rho}(\mathbf{r}') &= \hat{\rho}^{<}(\mathbf{r})\hat{\rho}^{<}(\mathbf{r}') \\ &+ \bar{\rho}^{>}(\mathbf{r})\hat{\psi}^{<\dagger}(\mathbf{r}')\hat{\psi}^{<}(\mathbf{r}') + \bar{\rho}^{>}(\mathbf{r}')\hat{\psi}^{<\dagger}(\mathbf{r})\hat{\psi}^{<}(\mathbf{r}) \\ &+ \underbrace{\hat{\psi}^{<\dagger}(\mathbf{r}) \langle \hat{\psi}^{>}(\mathbf{r})\hat{\psi}^{>\dagger}(\mathbf{r}') \rangle_0 \hat{\psi}^{<}(\mathbf{r}') + \hat{\psi}^{<}(\mathbf{r}) \langle \hat{\psi}^{>\dagger}(\mathbf{r}')\hat{\psi}^{>}(\mathbf{r}) \rangle_0 \hat{\psi}^{<\dagger}(\mathbf{r}')}_{(*)} \end{aligned}$$

with

$$\hat{\rho}^{<}(\mathbf{r}) = \hat{\psi}^{<\dagger}(\mathbf{r})\hat{\psi}^{<}(\mathbf{r}) \quad (\text{S27})$$

$$\bar{\rho}^{>}(\mathbf{r}) = \sum_{\substack{\sigma, n, \mathbf{k}; \\ E'_c < |\epsilon_{n, \mathbf{k}}| \leq E_c}} \phi_{\sigma n \mathbf{k}}^*(\mathbf{r})\phi_{\sigma n \mathbf{k}}(\mathbf{r}). \quad (\text{S28})$$

The first term gives the Coulomb e-e interaction between electrons of the slow modes  $\hat{\psi}^{<}(\mathbf{r})$  below the new cut-off  $E'_c$ . The second and third term could be omitted if the system has particle-hole (p-h) symmetry as in twisted bilayer graphene [55]. In our system described by Eq. (S21), the first nearest-neighbor coupling in  $\tilde{U}_d(\mathbf{G})$  preserves p-h symmetry. The p-h symmetry is broken if further-neighbor coupling is included, which is exponentially smaller [see Eq. (S20)]. So, it is legitimate in our RG derivation to neglect such weak p-h asymmetry in order to omit the second and the third term in the expansion.

Then, we evaluate the rest of the terms in the expansion, which represents precisely the correction to  $H_0$  from the

fast modes  $\hat{\psi}^>(\mathbf{r})$  via Coulomb e-e interactions. Let us write

$$\begin{aligned}
(*) &= \hat{\psi}^{<\dagger}(\mathbf{r}) \left( \sum_{\substack{\sigma, n, \mathbf{k}; \\ E'_c < \epsilon_{n, \mathbf{k}} \leq E_c}} \phi_{\sigma n \mathbf{k}}(\mathbf{r}) \phi_{\sigma n \mathbf{k}}^*(\mathbf{r}') \right) \hat{\psi}^{<}(\mathbf{r}') + \hat{\psi}^{<}(\mathbf{r}) \left( \sum_{\substack{\sigma, n, \mathbf{k}; \\ -E'_c > \epsilon_{n, \mathbf{k}} \geq -E_c}} \phi_{\sigma n \mathbf{k}}^*(\mathbf{r}) \phi_{\sigma n \mathbf{k}}(\mathbf{r}') \right) \hat{\psi}^{<\dagger}(\mathbf{r}') \\
&= \hat{\psi}^{<\dagger}(\mathbf{r}) \left( \sum_{\substack{\sigma, n, \mathbf{k}; \\ E'_c < \epsilon_{n, \mathbf{k}} \leq E_c}} \phi_{\sigma n \mathbf{k}}(\mathbf{r}) \phi_{\sigma n \mathbf{k}}^*(\mathbf{r}') \right) \hat{\psi}^{<}(\mathbf{r}') + \hat{\psi}^{<\dagger}(\mathbf{r}') \left( \sum_{\substack{\sigma, n, \mathbf{k}; \\ -E'_c > \epsilon_{n, \mathbf{k}} \geq -E_c}} -\phi_{\sigma n \mathbf{k}}^*(\mathbf{r}) \phi_{\sigma n \mathbf{k}}(\mathbf{r}') \right) \hat{\psi}^{<}(\mathbf{r})
\end{aligned}$$

where the minus sign in the second line comes from the exchange the two fermionic operators and the constant arising from the exchange is omitted. Then, the e-e interaction  $\hat{V}_{\text{int}}$  in the lower energy window delimited by  $E'_c$  is

$$\hat{V}_{\text{int}} = \frac{1}{2} \int d^2 \mathbf{r} d^2 \mathbf{r}' V_c(\mathbf{r} - \mathbf{r}') \hat{\rho}^{<}(\mathbf{r}) \hat{\rho}^{<}(\mathbf{r}') + \frac{1}{2} \int d^2 \mathbf{r} d^2 \mathbf{r}' V_c(\mathbf{r} - \mathbf{r}') \hat{\psi}^{<\dagger}(\mathbf{r}) \mathcal{F}(\mathbf{r}, \mathbf{r}') \hat{\psi}^{<}(\mathbf{r}') \quad (\text{S29})$$

with

$$\mathcal{F}(\mathbf{r}, \mathbf{r}') = \sum_{\substack{\sigma, n, \mathbf{k}; \\ E'_c < |\epsilon_{n, \mathbf{k}}| \leq E_c}} \text{sign}(\epsilon_{n, \mathbf{k}}) \phi_{\sigma n \mathbf{k}}(\mathbf{r}) \phi_{\sigma n \mathbf{k}}^*(\mathbf{r}'). \quad (\text{S30})$$

### Evaluation of the correction to the non-interacting Hamiltonian from the fast modes

In the following, we set  $\hbar = 1$  for the simplicity in mathematical expressions. Note that  $\mathcal{F}(\mathbf{r}, \mathbf{r}')$  has the structure of the residue of the Green's function  $\hat{G}(z) = (z - \hat{H}_0)^{-1}$  taking only the valley  $\mu = +1$  part in  $\hat{H}_0 = \hat{H}_G + \hat{H}_{G-S}$  [see Eqs. (S16) and (S19)], namely

$$\mathcal{F}(\mathbf{r}, \mathbf{r}') = \oint_{\mathcal{C}} \frac{dz}{2\pi i} \langle \mathbf{r} | \hat{G}(z) | \mathbf{r}' \rangle \quad (\text{S31})$$

where the contour  $\mathcal{C}$  encloses the  $z$ -plane real line segment  $[-E_c, -E'_c]$  in the clockwise, and segment  $[E'_c, E_c]$  in the counterclockwise, sense. As long as  $E'_c$  dominates over all other energy scales such as  $\tilde{U}_d(\mathbf{G}_0)$  and  $v_F G_0$  with  $\mathbf{G}_0$  denoting the primitive reciprocal vector of the underlying superlattice, the dominant contribution to the contour integral can be evaluated perturbatively using  $\hat{G}(z) \approx \hat{G}_0(z) + \hat{G}_0(z) \hat{H}_{G-S} \hat{G}_0(z) + \mathcal{O}(\tilde{U}_d^2(\mathbf{G}_0)/E_c^2, v_F^2 G_0^2/E_c^2)$  with  $\hat{G}_0(z) = (z - \hat{H}_G)^{-1}$ .

It is easier to calculate the Green's function in the plane wave basis  $|\mathbf{k}\rangle$

$$\mathcal{F}(\mathbf{r}, \mathbf{r}') = \int \frac{d^2 k d^2 k'}{(2\pi)^4} e^{i(\mathbf{k} \cdot \mathbf{r} - \mathbf{k}' \cdot \mathbf{r}')} \oint_{\mathcal{C}} \frac{dz}{2\pi i} \langle \mathbf{k} | \hat{G}(z) | \mathbf{k}' \rangle \quad (\text{S32})$$

with

$$|\mathbf{r}\rangle = \int \frac{d^2 k}{(2\pi)^2} e^{-i\mathbf{k} \cdot \mathbf{r}} |\mathbf{k}\rangle \quad (\text{S33})$$

$$\langle \mathbf{r} | \mathbf{r}' \rangle = \delta^{(2)}(\mathbf{r} - \mathbf{r}') \quad (\text{S34})$$

$$\langle \mathbf{k} | \mathbf{k}' \rangle = (2\pi)^2 \delta^{(2)}(\mathbf{k} - \mathbf{k}') \quad (\text{S35})$$

where  $\delta^{(2)}(\mathbf{x})$  is the 2D Dirac distribution. In the plane wave basis, the evaluation of Green's functions is straightforward

$$\langle \mathbf{k} | \hat{G}_0(z) | \mathbf{k}' \rangle = (2\pi)^2 \delta^{(2)}(\mathbf{k} - \mathbf{k}') \frac{1}{2} \sum_{\lambda=\pm} \frac{1 - \lambda \frac{\mathbf{k}}{k} \cdot \boldsymbol{\sigma}}{z - \lambda v_F k} \quad (\text{S36})$$

$$\langle \mathbf{k} | \hat{G}_0(z) \hat{H}_{G-S} \hat{G}_0(z) | \mathbf{k}' \rangle = (2\pi)^2 \delta^{(2)}(\mathbf{k} - \mathbf{k}' + \mathbf{G}) \frac{1}{4} \sum_{\mathbf{G}} \tilde{U}_d(\mathbf{G}) \sum_{\lambda, \lambda'=\pm} \frac{(1 - \lambda \frac{\mathbf{k}}{k} \cdot \boldsymbol{\sigma}) (1 - \lambda' \frac{\mathbf{k} + \mathbf{G}}{|\mathbf{k} + \mathbf{G}|} \cdot \boldsymbol{\sigma})}{(z - \lambda v_F k) (z - \lambda' v_F |\mathbf{k} + \mathbf{G}|)}. \quad (\text{S37})$$



Then, the contour integral can be easily done:

$$\oint_{\mathcal{C}} \frac{dz}{2\pi i} \langle \mathbf{r} | \hat{G}_0(z) | \mathbf{r}' \rangle = \int_{E'_c < v_F k \leq E_c} \frac{d^2 k}{(2\pi)^2} e^{i\mathbf{k} \cdot (\mathbf{r} - \mathbf{r}')} \frac{\mathbf{k}}{k} \cdot \boldsymbol{\sigma} \quad (\text{S38})$$

$$\oint_{\mathcal{C}} \frac{dz}{2\pi i} \langle \mathbf{r} | \hat{G}_0(z) \hat{H}_{G-S} \hat{G}_0(z) | \mathbf{r}' \rangle = \int_{E'_c < v_F k \leq E_c} \frac{d^2 k}{(2\pi)^2} e^{i\mathbf{k} \cdot (\mathbf{r} - \mathbf{r}') - i\mathbf{G} \cdot \mathbf{r}'} \frac{1}{4} \sum_{\mathbf{G}} \tilde{U}_d(\mathbf{G}) \mathcal{I}(\mathbf{k}, \mathbf{G}) \quad (\text{S39})$$

$$\mathcal{I}(\mathbf{k}, \mathbf{G}) = \frac{2}{v_F k + v_F |\mathbf{k} + \mathbf{G}|} \left( 1 - \frac{\mathbf{k} \cdot (\mathbf{k} + \mathbf{G})}{k |\mathbf{k} + \mathbf{G}|} + \frac{i\sigma_z (\mathbf{k} \times \mathbf{G}) \cdot \hat{\mathbf{z}}}{k |\mathbf{k} + \mathbf{G}|} \right). \quad (\text{S40})$$

### Renormalization group flow equations

Now we only have to insert the previous results into the second term in Eq. (S29) to derive the RG equations for  $v_F$  and  $\tilde{U}_d(\mathbf{G})$ . Let us compute first the integral for  $\langle \mathbf{r} | \hat{G}_0(z) | \mathbf{r}' \rangle$ . After writing the 2D Coulomb potential in Fourier space  $\tilde{V}_{2D}(\mathbf{q}) = e^2/2\epsilon_0\epsilon_r q$ , we have

$$\begin{aligned} & \frac{1}{2} \int d^2 \mathbf{r} d^2 \mathbf{r}' V_c(\mathbf{r} - \mathbf{r}') \oint_{\mathcal{C}} \hat{\psi}^{<\dagger}(\mathbf{r}) \frac{dz}{2\pi i} \langle \mathbf{r} | \hat{G}_0(z) | \mathbf{r}' \rangle \hat{\psi}^{<}(\mathbf{r}') \\ &= \int \frac{d^2 q}{(2\pi)^2} \hat{\psi}^{<\dagger}(\mathbf{q}) \underbrace{\left( \int_{E'_c < v_F k \leq E_c} \frac{d^2 k}{(2\pi)^2} \frac{e^2}{4\epsilon_0\epsilon_r} \frac{\mathbf{k}}{k} \cdot \boldsymbol{\sigma} \right)}_{(\text{A})} \hat{\psi}^{<}(\mathbf{q}) \end{aligned}$$

with  $\hat{\psi}^{<}(\mathbf{q})$  is the Fourier transform of  $\hat{\psi}^{<}(\mathbf{r})$ . Since  $v_F q \ll E'_c$ , we can Taylor expand (A) in terms of  $q/k$ . The leading order reads

$$(\text{A}) = \frac{e^2}{16\pi\epsilon_0\epsilon_r} \log\left(\frac{E_c}{E'_c}\right) \mathbf{q} \cdot \boldsymbol{\sigma}. \quad (\text{S41})$$

Therefore, the RG equation reads

$$\frac{dv_F}{d \log E_c} = -\frac{e^2}{16\pi\epsilon_0\epsilon_r}. \quad (\text{S42})$$

Actually, we find the famous result of the Fermi velocity renormalization in graphene due to the e-e interactions.

In the same way, we calculate the integral for  $\langle \mathbf{r} | \hat{G}_0(z) \hat{H}_{G-S} \hat{G}_0(z) | \mathbf{r}' \rangle$ :

$$\begin{aligned} & \frac{1}{2} \int d^2 \mathbf{r} d^2 \mathbf{r}' V_c(\mathbf{r} - \mathbf{r}') \oint_{\mathcal{C}} \hat{\psi}^{<\dagger}(\mathbf{r}) \frac{dz}{2\pi i} \langle \mathbf{r} | \hat{G}_0(z) | \mathbf{r}' \rangle \hat{\psi}^{<}(\mathbf{r}') \\ &= \int \frac{d^2 q}{(2\pi)^2} \hat{\psi}^{<\dagger}(\mathbf{q} - \mathbf{G}) \underbrace{\left( \int_{E'_c < v_F k \leq E_c} \frac{d^2 k}{(2\pi)^2} \tilde{V}_{2D}(\mathbf{q} - \mathbf{k} - \mathbf{G}) \frac{1}{8} \sum_{\mathbf{G}} \tilde{U}_d(\mathbf{G}) \mathcal{I}(\mathbf{k}, \mathbf{G}) \right)}_{(\text{B})} \hat{\psi}^{<}(\mathbf{q}). \end{aligned}$$

Since  $v_F q, v_F G \ll E'_c$ , we can Taylor expand (B) in terms of  $q/k$  and  $G/k$  (considered as if they have the same order of magnitude). The leading order reads

$$(\text{B}) = \frac{e^2}{16\epsilon_0\epsilon_r} G^2 \left( \frac{1}{E'_c} - \frac{1}{E_c} \right) + \mathcal{O}\left(\frac{v_F^3 q^3}{E_c'^3}, \frac{v_F^3 G^3}{E_c'^3}\right), \quad (\text{S43})$$

which can be neglected under the first-order RG procedure, namely

$$\frac{d\tilde{U}_d(\mathbf{G})}{d \log E_c} = 0. \quad (\text{S44})$$

In summary, we have shown that the Fermi velocity in graphene  $v_F$  is renormalized by the e-e Coulomb interaction in the standard way while the superlattice potential  $U_d(\mathbf{r})$  keep its value unchanged. In our numerical study of e-e

interactions, we use the renormalized Fermi velocity  $v_F^*$  in the Hartree-Fock calculations, where we have to take a cut-off  $n_{\text{cut}}$  to the number of bands, to include the contributions from the higher energy bands outside the cut-off. Technically, we use

$$v_F^* = v_F \left( 1 + \frac{e^2}{16\pi\epsilon_0\epsilon_r v_F} \log \left( \frac{L_s}{n_{\text{cut}} a_0} \right) \right) \quad (\text{S45})$$

where  $L_s$  and  $a_0$  are the lattice constant of the superlattice of  $U_d(\mathbf{r})$  and the carbon-carbon bond length in graphene, respectively. Here, the ratio  $L_s/n_{\text{cut}}a_0$  plays the role of  $E_c/E'_c$ .

### S3. HARTREE-FOCK APPROXIMATIONS TO ELECTRON-ELECTRON INTERACTIONS

The derivation shown in this section is inspired from Ref. 66. We consider the Coulomb interactions in graphene

$$\hat{V}_{\text{int}} = \frac{1}{2} \int d^2r d^2r' \sum_{\sigma, \sigma'} \hat{\psi}_{\sigma}^{\dagger}(\mathbf{r}) \hat{\psi}_{\sigma'}^{\dagger}(\mathbf{r}') V_{\text{int}}(|\mathbf{r} - \mathbf{r}'|) \hat{\psi}_{\sigma'}(\mathbf{r}') \hat{\psi}_{\sigma}(\mathbf{r}) \quad (\text{S46})$$

where  $\hat{\psi}_{\sigma}(\mathbf{r})$  is real-space electron annihilation operator at  $\mathbf{r}$  with spin  $\sigma$ . This interaction can be written as

$$\hat{V}_{\text{int}} = \frac{1}{2} \sum_{ii'jj'} \sum_{\alpha\alpha'\beta\beta'} \sum_{\sigma\sigma'} \hat{c}_{i,\sigma\alpha}^{\dagger} \hat{c}_{i',\sigma'\alpha'}^{\dagger} V_{ij,i'j'}^{\alpha\beta\sigma,\alpha'\beta'\sigma'} \hat{c}_{j',\sigma'\beta'} \hat{c}_{j,\sigma\beta}, \quad (\text{S47})$$

where

$$V_{ij,i'j'}^{\alpha\beta\sigma,\alpha'\beta'\sigma'} = \int d^2r d^2r' V_{\text{int}}(|\mathbf{r} - \mathbf{r}'|) \phi_{\alpha}^*(\mathbf{r} - \mathbf{R}_i - \tau_{\alpha}) \phi_{\beta}(\mathbf{r} - \mathbf{R}_j - \tau_{\beta}) \phi_{\alpha'}^*(\mathbf{r} - \mathbf{R}'_i - \tau_{\alpha'}) \phi_{\beta'}(\mathbf{r} - \mathbf{R}'_j - \tau_{\beta'}) \\ \times \chi_{\sigma}^{\dagger} \chi_{\sigma'}^{\dagger} \chi_{\sigma'} \chi_{\sigma}. \quad (\text{S48})$$

Here  $i, \alpha$ , and  $\sigma$  refer to Bravais lattice vectors, layer/sublattice index, and spin index.  $\phi$  is Wannier function and  $\chi$  is the two-component spinor wave function. We further assume that the "density-density" like interaction is dominant in the system, i.e.,  $V_{ij,i'j'}^{\alpha\beta\sigma,\alpha'\beta'\sigma'} \approx V_{ii,i'i'}^{\alpha\alpha\sigma,\alpha'\alpha'\sigma'} \equiv V_{i\sigma\alpha,i'\sigma'\alpha'}$ , then the Coulomb interaction is simplified to

$$\hat{V}_{\text{int}} = \frac{1}{2} \sum_{ii'} \sum_{\alpha\alpha'} \sum_{\sigma\sigma'} \hat{c}_{i,\sigma\alpha}^{\dagger} \hat{c}_{i',\sigma'\alpha'}^{\dagger} V_{i\sigma\alpha,i'\sigma'\alpha'} \hat{c}_{i',\sigma'\alpha'} \hat{c}_{i,\sigma\alpha} \\ = \frac{1}{2} \sum_{i\alpha \neq i'\alpha'} \sum_{\sigma\sigma'} \hat{c}_{i,\sigma\alpha}^{\dagger} \hat{c}_{i',\sigma'\alpha'}^{\dagger} V_{i\alpha,i'\alpha'} \hat{c}_{i',\sigma'\alpha'} \hat{c}_{i,\sigma\alpha} \\ + \sum_{i\alpha} U_0 \hat{c}_{i,\uparrow\alpha}^{\dagger} \hat{c}_{i,\downarrow\alpha}^{\dagger} \hat{c}_{i,\downarrow\alpha} \hat{c}_{i,\uparrow\alpha} \quad (\text{S49})$$

Here we can see that the Coulomb interaction can be divided into intersite Coulomb interaction and on-site Coulomb interaction. Given that the electron density is low ( $10^{11} \text{ cm}^{-2}$ ), i.e., a few electrons per supercell, the chance that two electrons meet at the same atomic site is very low. The Coulomb correlations between two electron are mostly contributed by the inter-site Coulomb interactions. Therefore, the on-site Hubbard interaction has been neglected in our calculations.

In order to model the screening effects to the e-e Coulomb interactions from the dielectric environment, we introduce the double gate screening form of  $V_{\text{int}}$ , whose Fourier transform is expressed as

$$V_{\text{int}}(\mathbf{q}) = \frac{e^2 \tanh(qd_s)}{2\Omega_0\epsilon_r\epsilon_0q}, \quad (\text{S50})$$

where  $\Omega_0$  is the area of the TMO superlattice's primitive cell,  $\epsilon_r$  is a background dielectric constant and the thickness between two gates is  $d_s = 400 \text{ \AA}$ .

Since we are interested in the low-energy bands, the intersite Coulomb interactions can be divided into the intra-valley term and the inter-valley term. The intra-valley term  $\hat{V}^{\text{intra}}$  can be expressed as

$$\hat{V}^{\text{intra}} = \frac{1}{2N_s} \sum_{\alpha\alpha'} \sum_{\mu\mu',\sigma\sigma'} \sum_{\mathbf{k}\mathbf{k}'\mathbf{q}} V_{\text{int}}(\mathbf{q}) \hat{c}_{\sigma\mu\alpha}^{\dagger}(\mathbf{k} + \mathbf{q}) \hat{c}_{\sigma'\mu'\alpha'}^{\dagger}(\mathbf{k}' - \mathbf{q}) \hat{c}_{\sigma'\mu'\alpha'}(\mathbf{k}') \hat{c}_{\sigma\mu\alpha}(\mathbf{k}), \quad (\text{S51})$$

with  $N_s$  is the total number of the superlattice's sites. The inter-valley term  $\hat{V}^{\text{inter}}$  is expressed as

$$\hat{V}^{\text{inter}} = \frac{1}{2N_s} \sum_{\alpha\alpha'} \sum_{\mu,\sigma\sigma'} \sum_{\mathbf{k}\mathbf{k}'\mathbf{q}} V_{\text{int}}(|\mathbf{K} - \mathbf{K}'|) \hat{c}_{\sigma\mu\alpha}^\dagger(\mathbf{k} + \mathbf{q}) \hat{c}_{\sigma' - \mu\alpha'}^\dagger(\mathbf{k}' - \mathbf{q}) \hat{c}_{\sigma'\mu\alpha'}(\mathbf{k}') \hat{c}_{\sigma - \mu\alpha}(\mathbf{k}) . \quad (\text{S52})$$

$\hat{V}^{\text{intra}}$  includes the Coulomb scattering processes of two electrons created and annihilated in the same valley, and  $\hat{V}^{\text{inter}}$  includes the processes that two electrons are created in  $\mu$  and  $-\mu$  and get annihilated in  $-\mu$  and  $\mu$  valleys. Here the atomic wavevector  $\mathbf{k}$  is expanded around the valley  $K^\mu$  in the big Brillouin zone of graphene, which can be decomposed as  $\mathbf{k} = \tilde{\mathbf{k}} + \mathbf{G}$ , where  $\tilde{\mathbf{k}}$  is the superlattice wavevector in the superlattice Brillouin zone, and  $\mathbf{G}$  denotes a superlattice reciprocal lattice vector.

The electron annihilation operator can be transformed from the original basis to the band basis:

$$\hat{c}_{\sigma\mu\alpha}(\mathbf{k}) = \sum_n C_{\sigma\mu\alpha\mathbf{G},n}(\tilde{\mathbf{k}}) \hat{c}_{\sigma\mu,n}(\tilde{\mathbf{k}}) , \quad (\text{S53})$$

where  $C_{\sigma\mu\alpha\mathbf{G},n}(\tilde{\mathbf{k}})$  is the expansion coefficient in the  $n$ -th Bloch eigenstate at  $\tilde{\mathbf{k}}$  of valley  $\mu$ :

$$|\mu, n; \tilde{\mathbf{k}}\rangle = \sum_{\alpha\mathbf{G}} C_{\sigma\mu\alpha\mathbf{G},n}(\tilde{\mathbf{k}}) |\sigma, \mu, \alpha, \mathbf{G}; \tilde{\mathbf{k}}\rangle . \quad (\text{S54})$$

We note that the non-interacting Bloch functions are spin degenerate due to the separate spin rotational symmetry ( $SU(2) \otimes SU(2)$  symmetry) of each valley. Using the transformation given in Eq. (S53), the intra- and inter-valley Coulomb interaction can be written in the band basis

$$\begin{aligned} \hat{V}^{\text{intra}} &= \frac{1}{2N_s} \sum_{\tilde{\mathbf{k}}\tilde{\mathbf{k}}'\tilde{\mathbf{q}}} \sum_{\mu\mu'} \sum_{\substack{n'm' \\ \sigma\sigma'}} \left( \sum_{\mathbf{Q}} V_{\text{int}}(\mathbf{Q} + \tilde{\mathbf{q}}) \Omega_{nm,n'm'}^{\mu\sigma,\mu'\sigma'}(\tilde{\mathbf{k}}, \tilde{\mathbf{k}}', \tilde{\mathbf{q}}, \mathbf{Q}) \right) \\ &\times \hat{c}_{\sigma\mu,n}^\dagger(\tilde{\mathbf{k}} + \tilde{\mathbf{q}}) \hat{c}_{\sigma'\mu',n'}^\dagger(\tilde{\mathbf{k}}' - \tilde{\mathbf{q}}) \hat{c}_{\sigma'\mu',m'}(\tilde{\mathbf{k}}') \hat{c}_{\sigma\mu,m}(\tilde{\mathbf{k}}) \end{aligned} \quad (\text{S55})$$

and

$$\begin{aligned} \hat{V}^{\text{inter}} &= \frac{1}{2N_s} \sum_{\tilde{\mathbf{k}}\tilde{\mathbf{k}}'\tilde{\mathbf{q}}} \sum_{\mu} \sum_{\substack{n'm' \\ \sigma\sigma'}} \left( \sum_{\mathbf{Q}} V_{\text{int}}(|\mathbf{K} - \mathbf{K}'|) \tilde{\Omega}_{nm,n'm'}^{\mu,\sigma\sigma'}(\tilde{\mathbf{k}}, \tilde{\mathbf{k}}', \tilde{\mathbf{q}}, \mathbf{Q}) \right) \\ &\times \hat{c}_{\sigma\mu,n}^\dagger(\tilde{\mathbf{k}} + \tilde{\mathbf{q}}) \hat{c}_{\sigma' - \mu,n'}^\dagger(\tilde{\mathbf{k}}' - \tilde{\mathbf{q}}) \hat{c}_{\sigma'\mu',m'}(\tilde{\mathbf{k}}') \hat{c}_{\sigma - \mu,m}(\tilde{\mathbf{k}}) \end{aligned} \quad (\text{S56})$$

where the form factors  $\Omega_{nm,n'm'}^{\mu\sigma,\mu'\sigma'}$  and  $\tilde{\Omega}_{nm,n'm'}^{\mu,\sigma\sigma'}$  are written respectively as

$$\Omega_{nm,n'm'}^{\mu\sigma,\mu'\sigma'}(\tilde{\mathbf{k}}, \tilde{\mathbf{k}}', \tilde{\mathbf{q}}, \mathbf{Q}) = \sum_{\alpha\alpha'\mathbf{G}\mathbf{G}'} C_{\sigma\mu\alpha\mathbf{G}+\mathbf{Q},n}^*(\tilde{\mathbf{k}} + \tilde{\mathbf{q}}) C_{\sigma'\mu'\alpha'\mathbf{G}'-\mathbf{Q},n'}^*(\tilde{\mathbf{k}}' - \tilde{\mathbf{q}}) C_{\sigma'\mu'\alpha'\mathbf{G}',m'}(\tilde{\mathbf{k}}') C_{\sigma\mu\alpha\mathbf{G},m}(\tilde{\mathbf{k}}) \quad (\text{S57})$$

and

$$\tilde{\Omega}_{nm,n'm'}^{\mu,\sigma\sigma'}(\tilde{\mathbf{k}}, \tilde{\mathbf{k}}', \tilde{\mathbf{q}}, \mathbf{Q}) = \sum_{\alpha\alpha'\mathbf{G}\mathbf{G}'} C_{\sigma\mu\alpha\mathbf{G}+\mathbf{Q},n}^*(\tilde{\mathbf{k}} + \tilde{\mathbf{q}}) C_{\sigma' - \mu\alpha'\mathbf{G}'-\mathbf{Q},n'}^*(\tilde{\mathbf{k}}' - \tilde{\mathbf{q}}) C_{\sigma'\mu'\alpha'\mathbf{G}',m'}(\tilde{\mathbf{k}}') C_{\sigma - \mu\alpha\mathbf{G},m}(\tilde{\mathbf{k}}) . \quad (\text{S58})$$

We make Hartree-Fock approximation to Eq. (S55) and Eq. (S56) such that the two-particle Hamiltonian is decomposed into a superposition of the Hartree and Fock single-particle Hamiltonians, where the Hartree term is expressed as

$$\begin{aligned} \hat{V}_H^{\text{intra}} &= \frac{1}{2N_s} \sum_{\tilde{\mathbf{k}}\tilde{\mathbf{k}}'} \sum_{\mu\mu'} \sum_{\substack{n'm' \\ \sigma\sigma'}} \left( \sum_{\mathbf{Q}} V_{\text{int}}(\mathbf{Q}) \Omega_{nm,n'm'}^{\mu\sigma,\mu'\sigma'}(\tilde{\mathbf{k}}, \tilde{\mathbf{k}}', 0, \mathbf{Q}) \right) \\ &\times \left( \langle \hat{c}_{\sigma\mu,n}^\dagger(\tilde{\mathbf{k}}) \hat{c}_{\sigma\mu,m}(\tilde{\mathbf{k}}) \rangle \hat{c}_{\sigma'\mu',n'}^\dagger(\tilde{\mathbf{k}}') \hat{c}_{\sigma'\mu',m'}(\tilde{\mathbf{k}}') + \langle \hat{c}_{\sigma'\mu',n'}^\dagger(\tilde{\mathbf{k}}') \hat{c}_{\sigma'\mu',m'}(\tilde{\mathbf{k}}') \rangle \hat{c}_{\sigma\mu,n}^\dagger(\tilde{\mathbf{k}}) \hat{c}_{\sigma\mu,m}(\tilde{\mathbf{k}}) \right) \end{aligned} \quad (\text{S59})$$

and

$$\begin{aligned} \hat{V}_H^{\text{inter}} = & \frac{1}{2N_s} \sum_{\tilde{\mathbf{k}}\tilde{\mathbf{k}}'} \sum_{\sigma\sigma'} \sum_{\substack{nm \\ n'm'}} \left( \sum_{\mathbf{Q}} V_{\text{int}}(|\mathbf{K} - \mathbf{K}'|) \tilde{\Omega}_{nm,n'm'}^{\mu,\sigma\sigma'}(\tilde{\mathbf{k}}, \tilde{\mathbf{k}}', 0, \mathbf{Q}) \right) \\ & \times \left( \langle \hat{c}_{\sigma\mu,n}^\dagger(\tilde{\mathbf{k}}) \hat{c}_{\sigma-\mu,m}(\tilde{\mathbf{k}}) \rangle \hat{c}_{\sigma'-\mu,n'}^\dagger(\tilde{\mathbf{k}}') \hat{c}_{\sigma'\mu,m'}(\tilde{\mathbf{k}}') + \langle \hat{c}_{\sigma'-\mu,n'}^\dagger(\tilde{\mathbf{k}}') \hat{c}_{\sigma'\mu,m'}(\tilde{\mathbf{k}}') \rangle \hat{c}_{\sigma\mu,n}^\dagger(\tilde{\mathbf{k}}) \hat{c}_{\sigma-\mu,m}(\tilde{\mathbf{k}}) \right). \end{aligned} \quad (\text{S60})$$

The Fock term is expressed as:

$$\begin{aligned} \hat{V}_F^{\text{intra}} = & -\frac{1}{2N_s} \sum_{\tilde{\mathbf{k}}\tilde{\mathbf{k}}'} \sum_{\substack{\mu\mu' \\ \sigma\sigma'}} \sum_{\substack{nm \\ n'm'}} \left( \sum_{\mathbf{Q}} V_{\text{int}}(\tilde{\mathbf{k}}' - \tilde{\mathbf{k}} + \mathbf{Q}) \Omega_{nm,n'm'}^{\mu\sigma,\mu'\sigma'}(\tilde{\mathbf{k}}, \tilde{\mathbf{k}}', \tilde{\mathbf{k}}' - \tilde{\mathbf{k}}, \mathbf{Q}) \right) \\ & \times \left( \langle \hat{c}_{\sigma\mu,n}^\dagger(\tilde{\mathbf{k}}') \hat{c}_{\sigma'\mu',m'}(\tilde{\mathbf{k}}') \rangle \hat{c}_{\sigma'\mu',n'}^\dagger(\tilde{\mathbf{k}}) \hat{c}_{\sigma\mu,m}(\tilde{\mathbf{k}}) + \langle \hat{c}_{\sigma'\mu',n'}^\dagger(\tilde{\mathbf{k}}) \hat{c}_{\sigma\mu,m}(\tilde{\mathbf{k}}) \rangle \hat{c}_{\sigma\mu,n}^\dagger(\tilde{\mathbf{k}}') \hat{c}_{\sigma'\mu',m'}(\tilde{\mathbf{k}}') \right). \end{aligned}$$

and

$$\begin{aligned} \hat{V}_F^{\text{inter}} = & -\frac{1}{2N_s} \sum_{\tilde{\mathbf{k}}\tilde{\mathbf{k}}'} \sum_{\substack{\sigma\sigma' \\ \mu}} \sum_{\substack{nm \\ n'm'}} \left( \sum_{\mathbf{Q}} V_{\text{int}}(|\mathbf{K} - \mathbf{K}'|) \tilde{\Omega}_{nm,n'm'}^{\mu,\sigma\sigma'}(\tilde{\mathbf{k}}, \tilde{\mathbf{k}}', \tilde{\mathbf{k}}' - \tilde{\mathbf{k}}, \mathbf{Q}) \right) \\ & \times \left( \langle \hat{c}_{\sigma\mu,n}^\dagger(\tilde{\mathbf{k}}') \hat{c}_{\sigma'\mu,m'}(\tilde{\mathbf{k}}') \rangle \hat{c}_{\sigma'-\mu,n'}^\dagger(\tilde{\mathbf{k}}) \hat{c}_{\sigma-\mu,m}(\tilde{\mathbf{k}}) + \langle \hat{c}_{\sigma'-\mu,n'}^\dagger(\tilde{\mathbf{k}}) \hat{c}_{\sigma-\mu,m}(\tilde{\mathbf{k}}) \rangle \hat{c}_{\sigma\mu,n}^\dagger(\tilde{\mathbf{k}}') \hat{c}_{\sigma'\mu,m'}(\tilde{\mathbf{k}}') \right). \end{aligned}$$

We note that the typical intravalley interaction energy  $\sim 240$  meV for  $L_s = 50$  Å and  $\epsilon_r = 3$ ; while the intervalley interaction  $\sim 30$  meV, which is one order of magnitudes smaller than the intravalley interaction, thus we neglect the intervalley term [see Eq. (S52)] in most of our calculations. We also check *a posteriori* that the intervalley Hartree and Fock energies are at least two orders of magnitude smaller than their intravalley counterpart. However, the intervalley interaction is crucial to lift the degeneracy between many-body ground state, namely their energy difference is within the convergence threshold  $10^{-8}$  eV. We show in the section of the Hartree-Fock results that it promotes topologically trivial Hartree-Fock ground states rather than topological Hartree-Fock ground states.

#### S4. NON-INTERACTING ENERGY BANDS AND THEIR TOPOLOGY

In this section, we show the non-interacting energy spectra and distributions of Berry curvature in the first Brillouin zone for  $L_s = 50, 200, 600 \text{ \AA}$  with  $r = 1.2$  and 3. Since the system preserves time-reversal symmetry and the superlattice potential  $U_d$  is diagonal in the sublattice subspace, the non-interacting energy spectrum in valley  $K'$  is exactly the same as that in valley  $K$  so that we only plot the spectrum for valley  $K$  here. As shown below, the distribution of Berry curvature of the highest valence and the lowest conduction band in valley  $K$  is exactly opposite to that in valley  $K'$  as another consequence of time-reversal symmetry of the system.

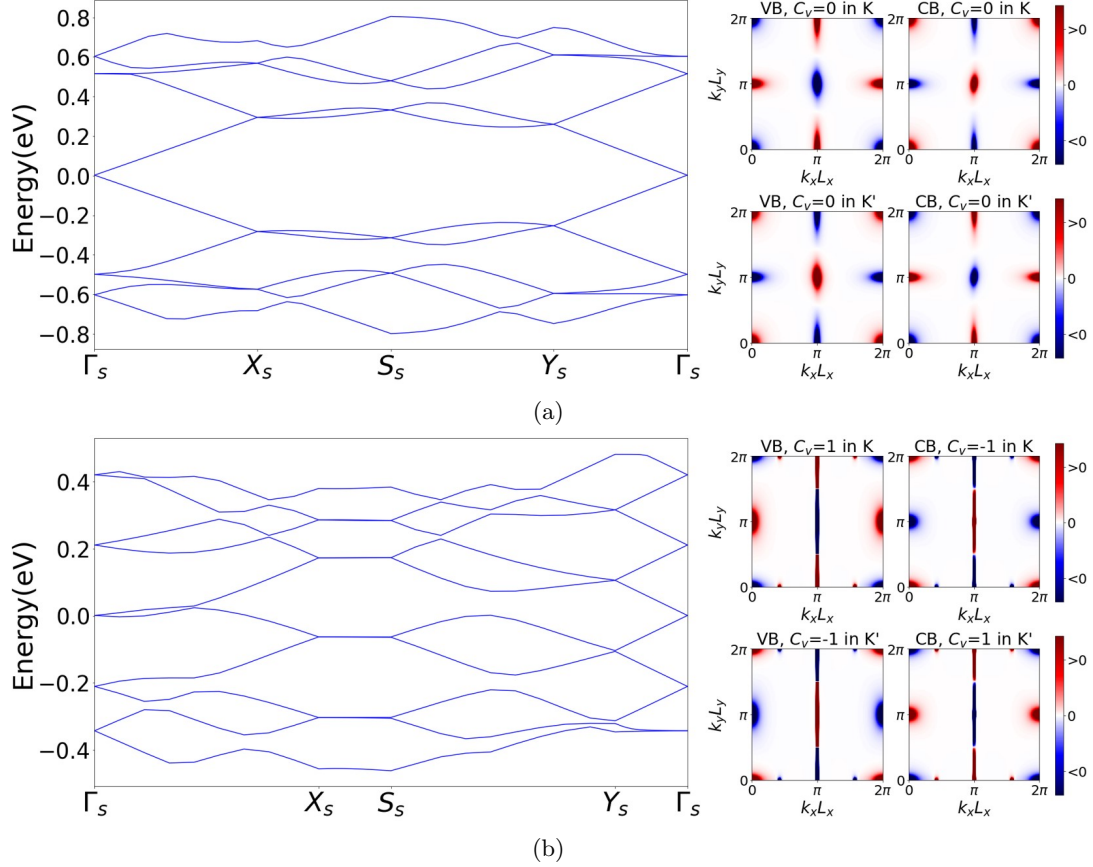


FIG. S1: Non-interacting spectrum and distribution of Berry curvature in the first Brillouin zone for  $L_s = 50 \text{ \AA}$  with (a)  $r = 1.2$  and (b)  $r = 3$ .

We also provide two videos in Supplemental Information, which shows the non-interacting energy spectra and distributions of Berry curvature in the first Brillouin zone for  $L_s = 50, 200, 600 \text{ \AA}$  with  $r = 1-10$ .

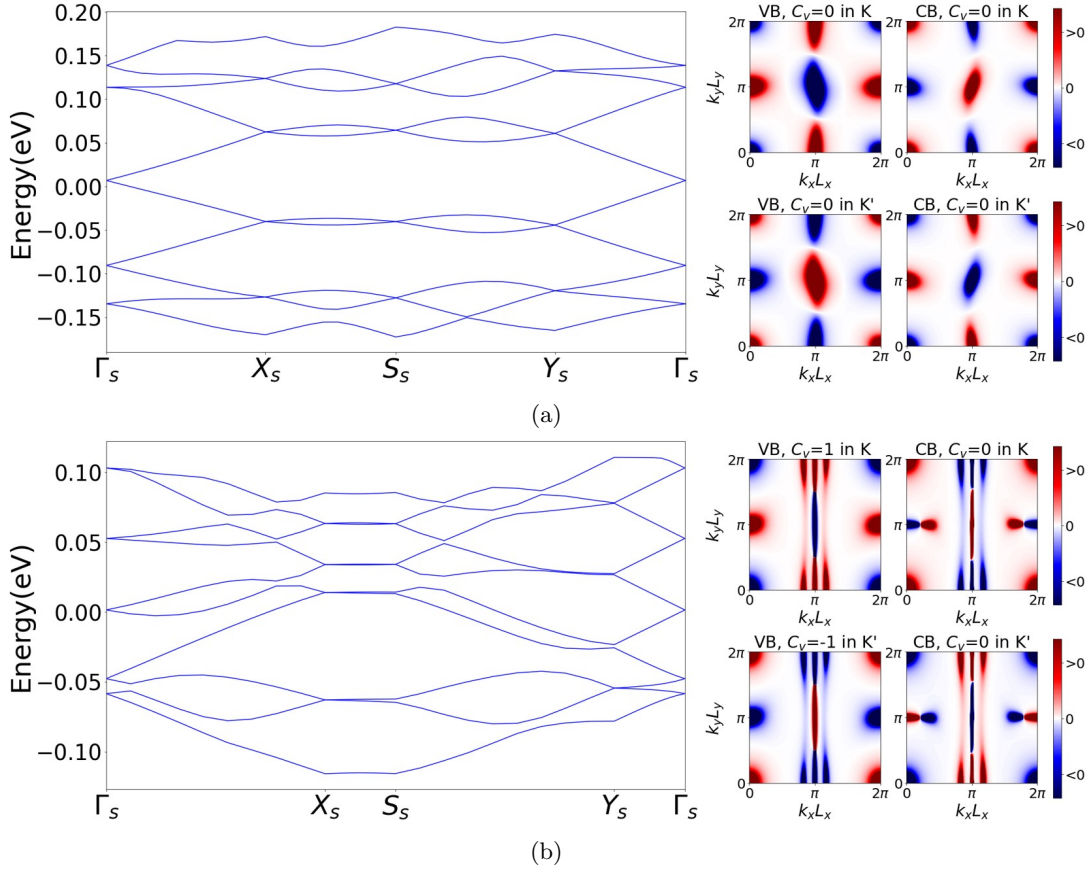


FIG. S2: Non-interacting spectrum and distribution of Berry curvature in the first Brillouin zone for  $L_s = 200 \text{ \AA}$  with (a)  $r = 1.2$  and (b)  $r = 3$ .

### S5. RESULTS OF HARTREE-FOCK CALCULATIONS

In this section, we gather the results of Hartree-Fock calculations including Hartree-Fock single-particle spectra and distributions of Berry curvature in the first Brillouin zone for  $L_s = 50, 200, 600 \text{ \AA}$ .

First, we show the Hartree-Fock single-particle spectrum with a superlattice potential with  $r = 1.2$  of  $L_s = 50, 200, 600 \text{ \AA}$ . Here, we use  $n_{\text{cut}} = 5$  and study three types of doping: CNP ( $\nu = 0$ ), slight hole doping ( $\nu = -0.003$ ) and slight electron doping ( $\nu = +0.003$ ). As you can see from Table I and the Hartree-Fock single-particle spectra, the results of a slightly electron-doped system is similar to those for a slightly hole-doped one. Note that we include only intravalley Coulomb interactions in these calculations. As shown in the following, the role of intervalley Coulomb interactions is merely to lift the ground state degeneracy and favor the topologically trivial ground state.

TABLE I: Parameters extracted from the Hartree-Fock single-particle spectra: gap opened at the CNP ( $\nu = 0$ ) and the ratio between interaction-renormalized Fermi velocity  $v_F^*$  and the non-interacting one  $v_F$  for different  $L_s = 50, 200, 600 \text{ \AA}$  with fixed  $r = 1.2$ .

$L_s(\text{\AA})$	50	200	600
Gap at $\nu = 0.0$ (meV)	17	1.7	0.15
$v_F^*/v_F$ at $\nu = -0.003$	2.1	1.8	1.7
$v_F^*/v_F$ at $\nu = +0.003$	2.1	1.8	1.7

Then, we show below the distributions of Berry curvature in the first Brillouin zone of  $r = 1.2$  for  $L_s = 50, 200, 600 \text{ \AA}$ . Here,  $n_{\text{cut}} = 5$ .

Now we show the effect of intervalley Coulomb interactions by comparing the total energy of topologically trivial



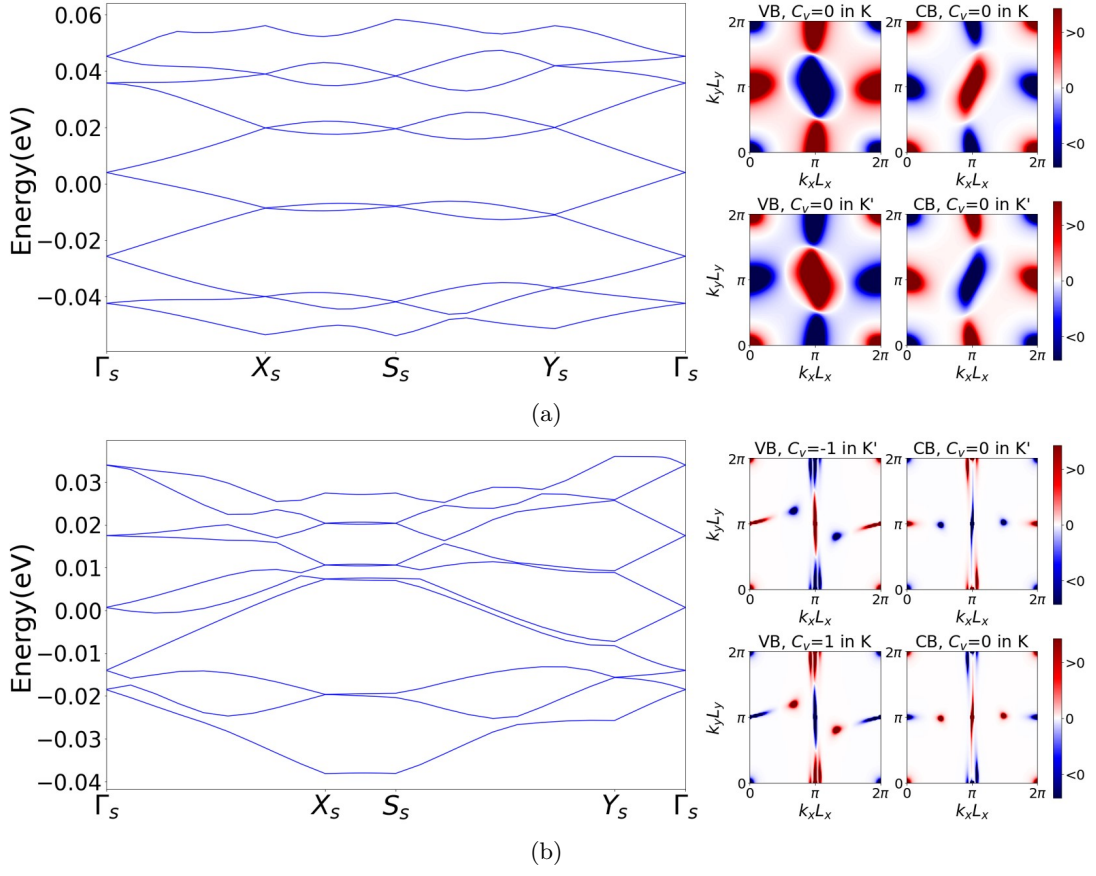


FIG. S3: Non-interacting spectrum and distribution of Berry curvature in the first Brillouin zone for  $L_s = 600 \text{ \AA}$  with (a)  $r = 1.2$  and (b)  $r = 3$ .

ground state with topological one for different  $L_s = 50, 200, 600 \text{ \AA}$  with fixed  $r = 1.2$ . We calculate the difference (always positive) between them and see how it changes when we include the intervalley Coulomb interactions. Here, we use  $n_{\text{cut}} = 3$ .

As you can see from Table II, the energy difference between the total energy of the topological ground state and topologically trivial one is enhanced by two orders of magnitude for  $L_s = 50$  and  $200 \text{ \AA}$ . However, the energy difference for  $L_s = 600 \text{ \AA}$  does not benefit anything from intervalley interactions. This suggests that it is plausible to find in practice the topological ground state if one achieves a rather low carrier density ( $\sim 10^{10} \text{ cm}^{-2}$ ) such that  $L_s = 600 \text{ \AA}$ .

$L_s(\text{\AA})$	50	200	600
$\Delta E$ with only intravalley ( $\mu\text{eV}$ )	0.024	0.005	0.05
$\Delta E$ with intra- and inter-valley ( $\mu\text{eV}$ )	1.7	0.1	0.03

TABLE II: Difference between the total energy of the topological ground state and topologically trivial one, with or without intervalley interactions, for  $L_s = 50, 200, 600 \text{ \AA}$  with fixed  $r = 1.2$ .

We also have performed Hartree-Fock calculations on a triangular lattice including three valence and three conduction bands ( $n_{\text{cut}} = 3$ ) for  $L_s = 50, 200, 600 \text{ \AA}$  using  $18 \times 18$   $k$ -mesh in the BZ. As shown in Table III, the results on a triangular lattice are qualitatively the same as those on a rectangular lattice. This ensures that our conclusions are lattice-independent.

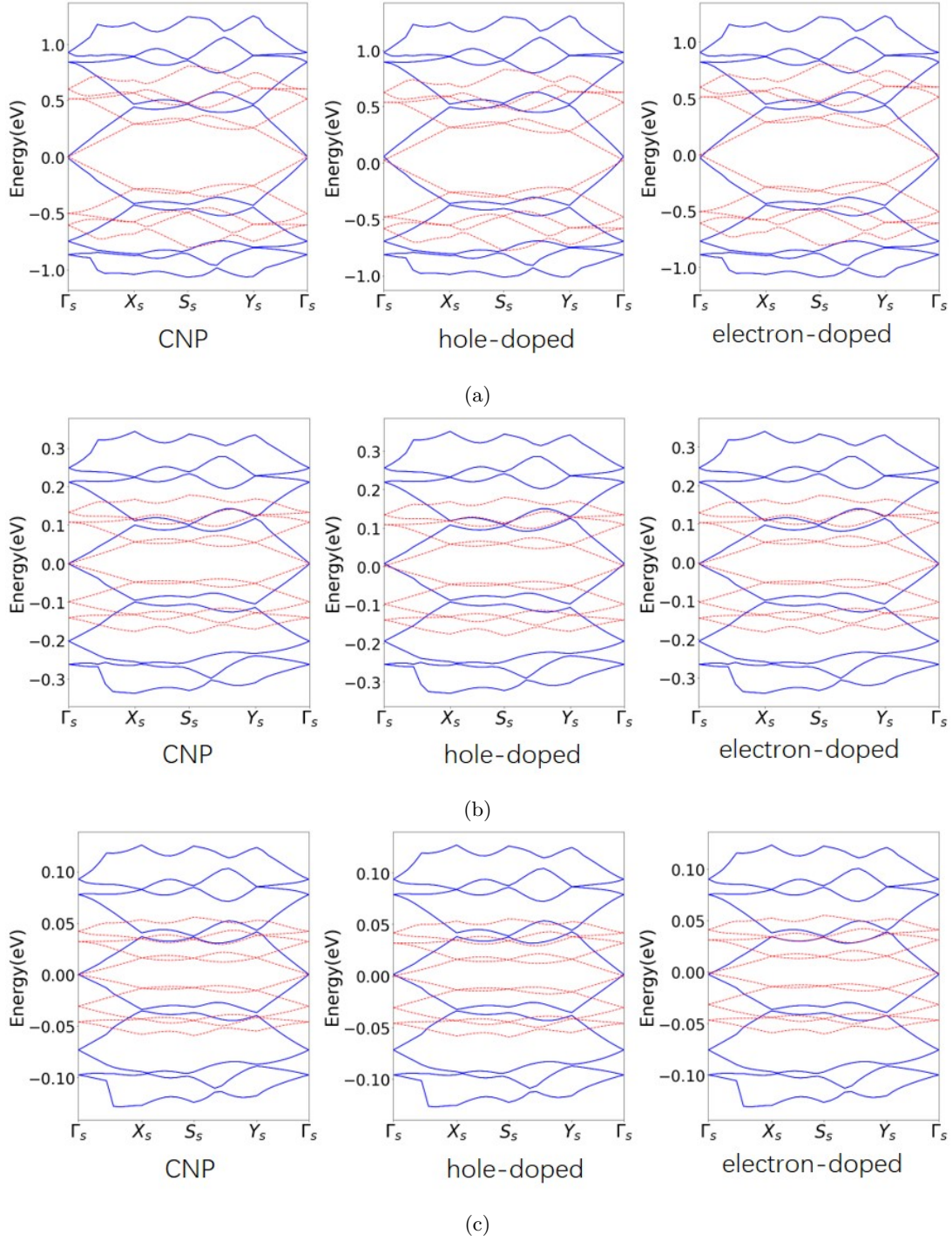


FIG. S4: Hartree-Fock single-particle spectra for three different dopings with  $r = 1.2$  for (a)  $L_s = 50 \text{ \AA}$ , (b)  $L_s = 200 \text{ \AA}$  and (c)  $L_s = 600 \text{ \AA}$ .

## S6 DETAILS OF DFT CALCULATIONS FOR THE SUBSTRATE MATERIALS

### Lattice structures, deformation potentials, and band structures of candidate substrate materials

In this section we present the details for the density function theory (DFT) calculations of the 11 candidate substrate materials presented in Table II of main text. The lattice structures of some of the substrate materials discussed in

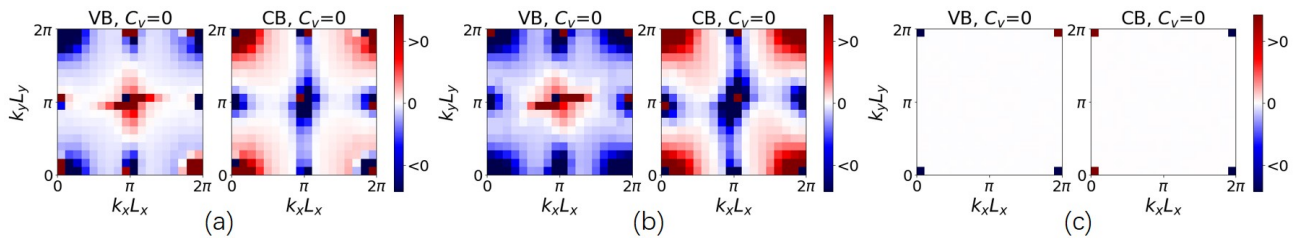


FIG. S5: Distributions of Berry curvature in the first Brillouin zone of  $r = 1.2$  for  $L_s =$  (a) 50 Å, (b) 200 Å, (c) 600 Å

TABLE III: Parameters extracted from the Hartree-Fock single-particle spectra on a triangular lattice: gap opened at the CNP ( $\nu = 0$ ) and the ratio between interaction-renormalized Fermi velocity  $v_F^*$  and the non-interacting one  $v_F$  for different  $L_s = 50, 200, 600$  Å.

$L_s$ (Å)	50	200	600
Gap at $\nu = 0.0$ (meV)	21	1.9	0.24
$v_F^*/v_F$ at $\nu = -0.003$	2.2	1.7	1.7

the main text are presented in Fig.S6. The lattice structure of  $\text{CrI}_3$  is similar to that of  $\text{YI}_3$  as shown in Fig. S6(d). The band structures of 10 candidate substrate materials (except for  $\text{CrOCl}$ ) in the bilayer or trilayer structures are presented in Fig. S7, where the green dashed lines mark the energy position of the Dirac point in graphene. We note that the valence band maximum (VBM) of  $\text{PbO}$  bilayer is energetically close to the Dirac point of graphene; while for the other bilayer or trilayer substrate materials, their conduction band minima (CBM) are close to the Dirac point. This indicates that charges can easily transferred between graphene and the substrates as controlled by gate voltages. Moreover, we note that the conduction bands and valence bands of these materials are typically flat with large effective masses, which would be very susceptible to  $e$ - $e$  Coulomb interactions once these substrate materials are slightly charge doped, and may to Wigner-crystal-like state or long-wavelength ordered state as discussed in main text. Another important precondition for the Wigner-crystal state is that the screening effect of substrate materials can not be too strong. For example, the conduction band of  $\text{ScOBr}$  bilayer has a large effective mass of  $2.575m_0$  ( $m_0$  is the bare mass of a free electron), but the dielectric constant  $\epsilon_d$  of  $\text{ScOBr}$  reaches  $\sim 13$ , which makes it difficult to form the Wigner-crystal-like instability in this material under slight charge doping.

We note that all of these proposed substrate materials all have been successfully synthesized in laboratory as listed in Table. IV. Especially, few-layer of  $\text{ReSe}_2$  as a highly anisotropic material [67–69], and few-layer  $\text{CrI}_3$  system as a 2D magnetic material [70–73], have been extensively studied recently. Moreover, phonon spectra calculations have proved the dynamical stability of these substrate materials in monolayer form [62]. Thus the device fabrication of heterostructure consisting of graphene monolayer and one of these candidate substrate materials should be experimentally accessible.

There always exists tension or compression in a heterostructure system. Under some lattice deformation, the variation of conduction band minimum (CBM) or valence band maximum (VBM) is defined as deformation potential. We list the deformation potentials of the candidate substrate materials in Table. IV. We note that the maximum value of the deformation potential is only 5.84 eV for  $\text{ScOCl}$ , which means that the energy level of CBM of  $\text{ScOCl}$  would move down by only 0.063 eV under 1% tensile strain. Therefore, even if strain is introduced in the graphene-insulator heterostructure proposed in this work, the band edges (with large effective masses) of those candidate substrate materials are still energetically close to the Dirac point of graphene.

In these candidate materials (except for  $\text{CrOCl}$ ),  $\text{CrI}_3$  bilayer is the only magnetic system. Previous theoretical studies reveal that the stacking configuration of  $\text{CrI}_3$  bilayer plays an important role in the magnetic ground state [74]. Here we use the  $\text{AB}'$ -type stacking in the bilayer structure, which is consistent with the stacking configuration in the bulk phase of  $\text{CrI}_3$ . The  $\text{AB}'$ -stacked  $\text{CrI}_3$  bilayer is in an intralayer ferromagnetic and interlayer antiferromagnetic ground state.

### Electric-field tunable band structures of bilayer CrOCl

Now we discuss the electronic structure of CrOCl bilayer under vertical electrical fields. Here we consider an intralayer ferromagnetic and interlayer antiferromagnetic state for the bilayer configuration, which turns out to be one of competing low-energy magnetic states, and is the magnetic ground state when the on-site Hubbard  $U$  value for the Cr  $3d$  orbitals is large. [75] The calculated band gap of CrOCl bilayer with the DFT+ $U$  calculation is 3.13 eV, which is close to that of HSE06 calculation (3.12 eV) [62]. The band structure of antiferromagnetic CrOCl bilayer is shown in Fig. S8(a), where the green dashed line marks the energy position of the Dirac point of graphene. Without vertical electric field, the Dirac point is slightly above the CBM of bilayer CrOCl. Applying a vertical electric field of 0.03 V/nm would push down the CBM as shown in Fig. S8(b). A closer inspection reveals that the top-layer conduction state (red lines) is pushed downwards while the bottom-layer state (blue lines) is pushed upward in energy as shown in Fig. S8(b), such that electron carriers in the graphene layer (if there is any) would be transferred to the top layer of CrOCl substrate, forming a Wigner-crystal-like state at the surface of CrOCl substrate given that the Wigner-Seitz radius of the CBM  $\sim 39$  is above the threshold value  $\sim 30$  (see Table. II in main text). Thus, our conjecture is supported by detailed first principles DFT calculations.

In Fig. S8(c) we also present the Fermi surfaces at different Fermi energies above the CBM of bilayer CrOCl. At very low carrier densities with small Fermi energy (CBM is set to zero), the Fermi surface consists of two nearly isotropic circles. For example, at filling factor 1/100 (corresponding to a carrier density  $\sim 8 \times 10^{12} \text{ cm}^{-2}$ ), the Fermi surface is marked by the red circles. Such isotropic Fermi surface with large effective mass ( $\sim 1.308m_0$ ) is likely to give rise to Wigner-crystal state as discussed in main text. As the Fermi level further increases, the Fermi surfaces become more and more anisotropic.

TABLE IV: The experimental works about the ten substrate materials, and the uni-axial deformation potentials of these materials [62].

Materials	References	Deformation potentials
AgScP <sub>2</sub> S <sub>6</sub>	Ref. [76]	–
AgScP <sub>2</sub> Se <sub>6</sub>	Ref. [77]	–
IrBr <sub>3</sub>	Ref. [78]	-3.76 eV
IrI <sub>3</sub>	Ref. [79]	-2.17 eV
YI <sub>3</sub>	Ref. [80]	1.47 eV
YBr <sub>3</sub>	Ref. [81]	1.43 eV
ReSe <sub>2</sub>	Ref. [82]	-4.45 eV
ScOCl	Ref. [83]	-5.84 eV
PbO	Ref. [84]	-4.60 eV
CrI <sub>3</sub>	Ref. [70–73]	-2.20 eV

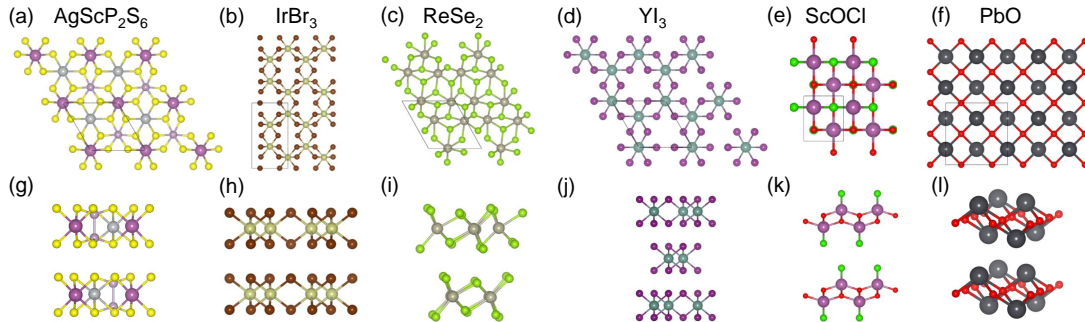


FIG. S6: (a)-(f): top views of the lattice structures of some candidate substrate materials in monolayer form. The primitive cells are remarked with black lines. (g)-(l): the side views of these substrate materials in few-layer form.



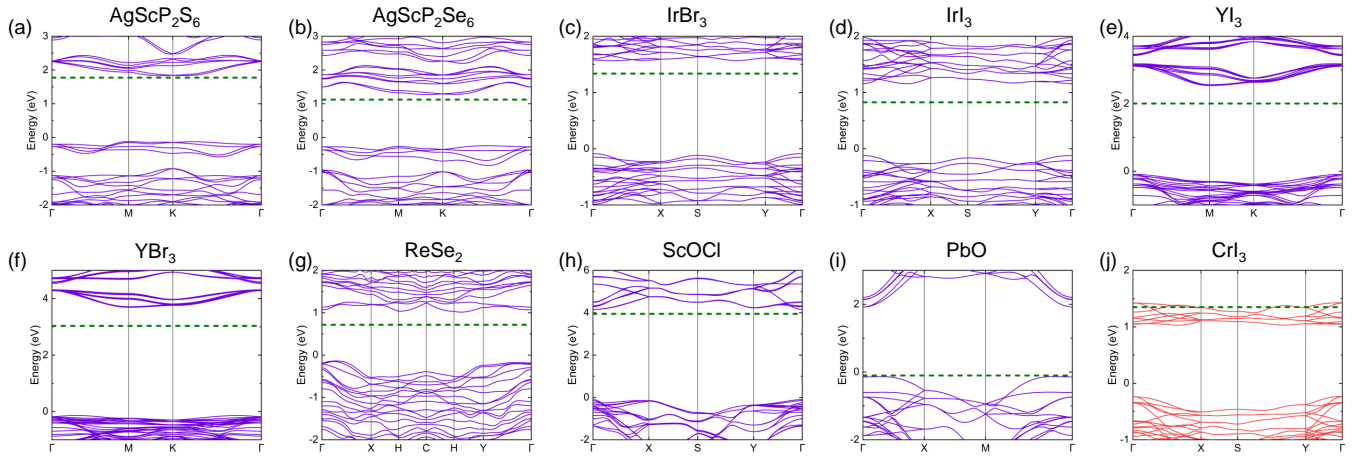


FIG. S7: The calculated energy bands of the candidate substrate materials, where the energy position of the Dirac point of graphene is marked by a dashed green line in the band structure.

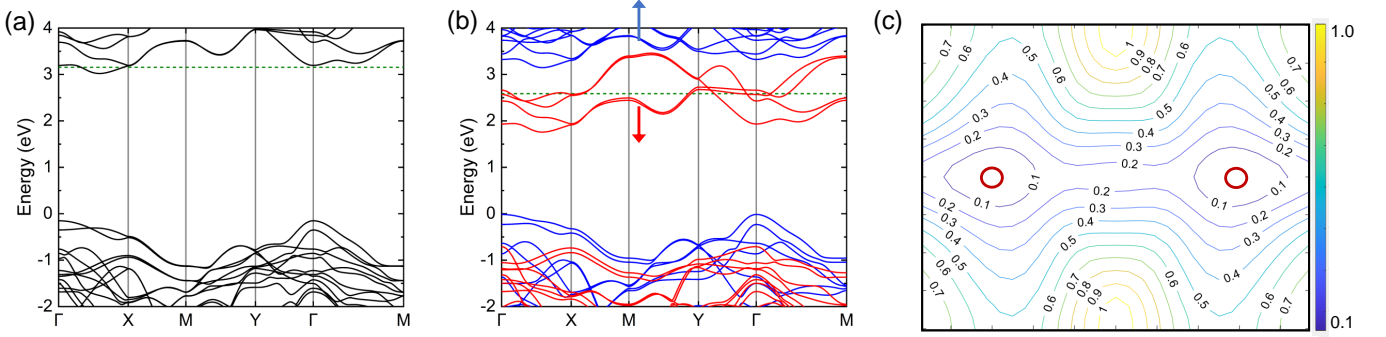


FIG. S8: The calculated energy bands of antiferromagnetic bilayer CrOCl: (a) without electric field, and (b) with an electric field  $0.03 \text{ V/nm}$ . In (b), the energy bands from top and bottom layers are marked by red and blue lines, respectively. The energy position of the Dirac point of graphene are remarked with green dashed lines. (c) Fermi surface of bilayer CrOCl at different Fermi levels with respect to the conduction band minimum. The Fermi surface under  $1/100$  electron filling factor is remarked by red circles.